Understanding steady and dynamic shear banding in a model wormlike micellar solution

Michelle A. Calabrese[†], Simon A. Rogers[†], Lionel Porcar[‡], and Norman J. Wagner[†*]
[†] *Center for Neutron Science, Department of Chemical and Biomolecular Engineering,*
University of Delaware, Newark, Delaware 19716
[†] *Department of Chemical and Biomolecular Engineering,*
University of Illinois Urbana-Champaign, Urbana, Illinois 61801
[‡] *Institute Laue-Langevin, BP 156, F38042 Grenoble Cedex 9, France*

Shear banding under steady and dynamic deformation is examined using a combination of rheology and flow-small angle neutron scattering (SANS) in a model wormlike micelle (WLM) solution comprised of a mixed cationic/anionic surfactant (CTAT/SDBS) and sodium tosylate (NaTos). Flow-vorticity plane rheo-SANS reveal long transients during shear band formation. Flow-gradient plane spatially resolved flow-SANS measurements probe the microstructure during steady and dynamic shear banding. Under large amplitude oscillatory shear (LAOS) deformation, shear banding is dependent on the Deborah and Weissenberg numbers, validating recent theoretical predictions that include shear-induced breakage. Micelle segmental alignment in the flow-gradient plane during LAOS is a non-monotonic function of cycle time, t/T, and radial position, r/H. The maximum segmental alignment under LAOS often exceeds that of the corresponding shear rate under steady shear, termed 'over-orientation,' which can help identify LAOS shear banding. The results of this study present new methods for identifying shear banding under steady and dynamic deformation, while providing an extensive data set for the development and further improvement of constitutive models.

[*] Corresponding Author: wagnernj@udel.edu

I. INTRODUCTION

Wormlike or polymer-like micelles (WLMs/PLMs) are a commonly used model system for studying non-linear flow phenomena and flow instabilities such as shear banding [1–3]. Linear WLMs tend to exhibit shear banding under steady shear deformation, a phenomenon where the flow exhibits spatial heterogeneities and organizes into macroscopic bands of high shear rate (low viscosity) and low shear rate (high viscosity). By altering the WLM solution composition or temperature, morphological changes can be induced and controlled [4–6]. These structural changes, such as changes in the branching density or contour length, have been shown to lower the zero-shear viscosity, η_0, of the solution [7–10]. Branching in WLMs has shown the potential to alter or eliminate the shear banding behavior of the solution, as the apparent 'stress plateau' increases in slope with increasing branching [11]. Shear banding occurs in systems that have an underlying non-monotonic constitutive equation [12,13]. However, shear banding has also been observed in models of entangled polymers and in WLMs that exhibit monotonic flow curves [14,15]. Accordingly, the steady shear flow curve of most shear banding WLMs can be described by three regions: the low shear rate Newtonian regime (region I), shear banding regime (region II), and the regime at shear rates in excess of the shear banding regime (region III).

Shear banding has been verified experimentally in polymeric and micellar systems using a variety of experimental methods. Rheo-optical flow birefringence [3,16] and rheo-nuclear magnetic resonance (rheo-NMR) measurements [17,18] were some of the first methods used to observe shear banding in WLM solutions. Direct imaging methods, such as particle tracking velocimetry (PTV), have shown the formation of transient and steady shear bands [19,20]. Scattering methods including flow-small angle neutron, light or x-ray scattering (flow-SANS, flow-SALS, flow-SAXS) are also commonly used when determining signatures of shear banded flow [21–24]. Berret *et al.* [21] first used rheo-SANS in the flow-vorticity (1-3) plane to estimate the width of the shear bands in a WLM solution. Spatially-resolved SANS measurements in the flow-gradient (1-2) plane were later used to detect shear banding [6,23,25–27]. In these works, shear banding was confirmed by a large decrease in micelle segmental alignment across the concentric-cylinder Couette cell gap. The discontinuous material alignment as a function of increasing gap position led to a high 'alignment band' and low 'alignment band' that corresponded to the high and low shear rate bands. Helgeson *et al.* [25] used a combination of flow-SANS and rheo-PTV to determine a critical alignment factor and angle at the shear band interface, which has shown to be applicable to other shear banding WLM solutions [27]. In highly shear thinning, non-shear banding materials, the alignment slowly and gradually decreased as a function of gap position [6,25,28] and did not meet the critical values necessary for shear banding set forth by Helgeson *et al.* [25]. Several phenomena have been commonly observed in shear banding materials, including slow transients, the formation of shear-induced structures, and oscillating rheological responses [15,29,30], which may include elastic turbulence and fluctuations of the shear band interface [31–33]. These rheological characteristics and experimental techniques are detailed in a review by Manneville [34]. The majority of this experimental work, however, focuses on shear banding under steady shear flow. Shear banding and related flow instabilities have been widely predicted under dynamic flows such as large amplitude oscillatory shear (LAOS). Constitutive models have been used to identify Deborah number ($De = \tau_R\omega$) and Weissenberg number ($Wi = \tau_R\dot{\gamma}$) conditions for transient or steady shear banding in concentric-cylinder Couette flow during LAOS, where ω is the applied angular frequency of the oscillation and τ_R is the relaxation time and inverse of the cross-over frequency ($\tau_R = 1/\omega_c$) [14,35]. Other works have suggested shear banding or similar instabilities under LAOS by showing that a material may act simultaneously as a fluid and elastic solid during LAOS, depending on the gap position [36,37].

Recent experiments have probed LAOS conditions where shear banding may occur; however, experimental verification of shear banding under LAOS is limited. In entangled polymer solutions, shear banding was observed for several Deborah numbers greater than one [38–40]. However, these results were debated by Li *et al.* [41], who used the same solutions to show that significant edge effects may have induced the shear banding. In wormlike micelles under LAOS, shear banding was observed at low Deborah and Weissenberg numbers at the onset of non-linearity [42]. In all of these works, rheo-PTV was used to confirm shear banding using a cone and plate geometry, whereas the model predictions of Adams and Olmsted [14] and Zhou *et al.* [35] are for concentric-cylinder Couette flow. To date, experimental work examining shear banding under LAOS in a concentric-cylinder Couette geometry is limited. Additionally, the previously cited works have only examined two regimes: high frequency (high De) or low frequency, low shear rate (low De and Wi). Thus the higher Weissenberg number conditions where shear banding may be present, as predicted by Zhou *et al.* [35], has not been verified, nor has any work used a method other than rheo-PTV to identify dynamic shear banding. Lastly, recent experimental work by Gurnon *et al.* [27] examining WLMs under LAOS was unable to verify the predictions of the Vasquez-Cook-McKinley (VCM) model used by Zhou *et al.* [35]. In this work, no shear banding was observed at De = 2.3 and Wi = 23 in a concentric-cylinder Couette shear cell, a condition clearly within the banding region identified with the VCM model. However, differences in the underlying flow curves are likely the cause of this discrepancy, as the solution used by Gurnon *et al.* [27] also did not show shear banding under steady shear at Wi = 23. The other two LAOS conditions probed by Gurnon *et al.* [27] were near the beginning of the shear banding regime (region II), and neither displayed shear banding, despite shear banding at these rates under steady shear. These latter conditions, in conjunction with the VCM model predictions, illustrate that the presence of LAOS shear banding is dependent on the applied frequency and amplitude.

Here, we aim to further explore the shear banding under steady and dynamic deformation in a WLM solution with a strictly increasing, monotonic flow curve that closely resembles the flow curve used in the VCM model predictions. To investigate the shear banding behavior, we use nonlinear rheology and neutron scattering techniques (flow-SANS) with spatial and temporal resolution [43]. Such neutron methods enable us to determine the time-dependent microstructural transitions that affect the macroscopic shear banding behavior [44]. The solution is composed of mixed cationic and anionic surfactants cetyltrimethylammonium tosylate (CTAT) and sodium dodecyl benzene sulfonate (SDBS) near the overlap concentration ($C^{*}\approx C_D$=1.5% wt) with 0.05% wt hydrotropic salt, sodium tosylate (NaTos). The rheology, phase behavior, and microstructural length scales have been extensively studied [4]. This NaTos concentration lies between two NaTos concentrations previously characterized by cryo-TEM: 0.01% wt (no observable branch points) and 0.10% wt (many observable branch points), in a salt concentration regime where the branch density increases with decreasing η_0 [8], indicating a likelihood of mild branching at this salt concentration [6]. For C_s = 0.01% wt NaTos, shear banding was confirmed in region II under steady shear deformation; at C_s = 0.10% wt NaTos, no shear banding occurred in region II [6]. The choice of this composition enables a quantitative comparison with theoretical predictions for shear banding under LAOS [35]. In this manuscript, we focus on shear banding under steady shear and LAOS at shear rates near the transition from region II to region III of the flow curve, explore the effect of De and Wi on LAOS shear banding, and validate recent predictions of LAOS shear banding [35].

II. THEORY

Cates and co-workers used a theory of breakage and recombination for nonionic micelles to extract critical parameters for the onset of shear banding under steady shear deformation [1, 45, 46]. For a given plateau modulus, G_N^0, and material relaxation time, τ_R, the critical stress, σ_1, and shear rate, $\dot{\gamma}_1$ or Wi_1, for the onset of shear banding are predicted by Equation 1:

$$\sigma_1 = 2/3G_N^0 \quad \dot{\gamma}_1 = 2.6/\tau_R \ \text{ or } \ Wi_1 = 2.6 \tag{1}$$

Deviations may result in the case of charged or branched micelles, where this model is no longer strictly applicable [4,11,47]. Koshy *et al.* [47] showed that the scaling of G_N^0 with concentration is stronger in regimes where branching is not expected, which may lead to discrepancies in the critical shear rate and stress predictions. Additionally, Fardin *et al.* [33] demonstrated that solution temperature and composition can affect these critical stress and shear rate values. It is widely accepted that the band width in the shear banding regime increases linearly with applied shear rate, as shown by several theoretical and experimental works [1, 17, 26, 48]. The applied shear rate, $\dot{\gamma}$ or Wi, results from the proportion of the material in the high shear ($\dot{\gamma}_2$, Wi_2) and low shear ($\dot{\gamma}_1$, Wi_1) rate bands:

$$\dot{\gamma} = (1-\alpha)\dot{\gamma}_1 + \alpha\dot{\gamma}_2 \ \text{ or } \ Wi = (1-\alpha)Wi_1 + \alpha Wi_2 \tag{2}$$

where α is the fraction of the material within the high shear rate, or ‘high shear,’ band, $\dot{\gamma}_1$ or Wi_1 is the shear rate at the onset of region II, and $\dot{\gamma}_2$ or Wi_2 is the shear rate at the onset of region III.

In many micellar and polymeric solutions, Equation 2 successfully describes the shear banding behavior of the system [38,49]. Experiments have shown that in some solutions, the average shear rate in the high and low shear bands increases with increasing applied shear rate; however, these changes are fairly small [19,26]. In all of these works, the linear relationship between shear rate and band width was confirmed. While significant theoretical work has been dedicated to steady shear banding, modeling efforts to predict shear banding under large amplitude oscillatory shear have been limited. Adams and Olmsted [14] used the Rolie-Poly (RP) model with a convected constraint release term, and predicted De and Wi values where inhomogeneous and homogeneous flow were expected under LAOS in the range of $1 \leq De \leq 100$ and $5 \leq Wi \leq 100$. Zhou *et al.* [35] used the Vasquez-Cook-McKinley (VCM) model to predict shear banding under LAOS with specific model parameters, and compared their results with a simpler, limiting case of the model. Unlike the RP model that attributes shear banding to flow-induced micellar alignment [50], the VCM model explicitly accounts for micellar breakage that leads to shear banding [51,52]. Both groups examined a broad range of De, Wi, and critical strain ($\gamma_{0,c}$) conditions and identified where shear banding may occur covering the range $0.1 \leq De \leq 25$, $0.1 \leq Wi \leq 500$ and $1 \leq \gamma_{0,c} \leq 1000$, yielding similar results.

Equations 1 and 2 are difficult to interpret in the context of oscillatory deformations, as the applied shear rate, and consequently gap-averaged shear rate, is constantly varying throughout the cycle [53]. Further, the LAOS 'steady alternance' stress response can correspond to a metastable structural state unobtainable under steady shear conditions [27]. In this work, we probe LAOS states where the VCM model predicts shear banding and use direct measurements of the spatiotemporal micellar segmental alignment to test the model predictions. In addition, by comparing the degree of micellar alignment under LAOS to that during steady shear, we observe a dramatic level of 'over-orientation' for some conditions. The complex local variations in micellar alignment during the oscillation cycle are compared to the highly non-linear rheological response to provide insights into the structure-property relationships for entangled WLMs, as well as quantitative data for testing rheological models based on micellar dynamics.

III. MATERIALS AND METHODS

A. Materials

The WLM system presented was previously well-characterized over a range of added salt concentrations [4,6,11]. The specific WLM solution is composed of mixed cationic and anionic surfactants CTAT and SDBS in D_2O with a total surfactant concentration held constant at 1.5% wt (97/3 weight ratio of CTAT/SDBS; 35.8 mM CTAT/1.45 mM SDBS) and a sodium tosylate (NaTos) content of 0.05% wt NaTos. Sodium tosylate and CTAT were obtained from Sigma-Aldrich. CTAT was recrystallized twice from a 50/50 mixture of ethanol and acetone. Sodium tosylate was used as received. Soft-type (linear chain) SDBS was obtained from TCI and used as received. All samples were prepared at room temperature in D_2O (Cambridge Isotopes, 99.8%) that was filtered before use. Samples were kept at 35 °C for three days before performing SANS or rheological measurements to ensure chemical, kinetic, and thermal stability. All measurements are performed at 35 °C to avoid crystallization at room temperature.

B. Rheometry

All rheometry measurements were performed at 35 °C ± 0.1 °C on an ARES G2 strain-controlled rheometer (TA Instruments, New Castle, DE) with temperature control from a ThermoCube circulating chiller (AMS Technologies). A concentric-cylinder Couette geometry was used with a stationary inner cylinder, stainless steel DIN bob (R_1 = 13.84 mm) and a rotating outer cylindrical cup (R_2 = 15.00 mm), such that the gap width, H, was 1.16 mm. Using the length of the Couette bob, L, the resulting aspect ratio, Γ = L/H, was 35 and the gap to radius ratio, ε = H/R_1, was 0.084. Rheological measurements were repeated during SANS on an Anton-Paar MCR-501 stress-controlled rheometer operating in strain-controlled mode, with a solvent trap filled with D_2O to provide a saturated atmosphere. A concentric-cylinder Couette geometry with a moving inner cylinder and stationary outer cup was used, where R_1 = 13.5 mm, R_2 = 14.5 mm, ε = 0.074, and Γ = 36. Samples were conditioned in the rheometer for 10 minutes at 35 °C to achieve thermal equilibrium. Frequency sweeps were then performed using a strain amplitude of 5% to measure the linear viscoelastic response of each sample. The delay time between measurements was at least $10\tau_R$. Initial sweeps were performed in triplicate over the course of one hour to ensure structural and thermal equilibrium after loading. Sweeps were performed over a frequency range of ω = 0.1 to 20 rad $\cdot$ s^{-1} (increasing and decreasing) with no observable hysteresis. Steady shear flow sweeps were performed to measure the steady-state material viscosity and stress over a range of shear rates (0.1 - 1000 s^{-1}). Sweeps were performed in the increasing and decreasing directions with at least $10\tau_R$ of rest time between each datum without observable hysteresis. The steady state flow curves were verified with long-time (300 - 5400 s) startup measurements of the stress. LAOS measurements were performed from startup to steady state with greater than $10\tau_R$ of delay time between experiments, over multiple cycles until steady alternance was reached. Conditions were repeated to ensure reproducibility (see Supporting Information). Frequency sweeps were performed after each rheological test to confirm the absence of foaming, evaporation, or irreversible changes from shear. Rheology was verified to be independent of instrument and geometry.

C. SANS measurements

1. Static SANS

Static SANS measurements were taken at the National Institute of Standards and Technology (NIST) Center for Neutron Research in Gaithersburg, MD on the NG-7 30 m SANS instrument. Samples were measured in 2 mm quartz cells with temperature control set to 35 °C ± 0.1 °C. The measured scattering vector, q, ranged from 0.001 Å^{-1} to 0.5 Å^{-1} using detector distances of 15.3 m (lens), 4 m and 1 m. The neutron wavelength, λ, was 6 Å at 4 m and 1 m, and 8.4 Å at 15.3 m. The wavelength spread, $\Delta\lambda/\lambda$, was 11.5% for both wavelengths. Raw data was reduced to an absolute scale as outlined by NIST standards by accounting for background, empty cell scattering, and detector efficiency [54]. Absolute scattering profiles were shown to be independent of instrument and sample environment from additional SANS experiments at NIST and on the D-22 instrument in the 1-2 shear cell at the Institut Laue-Langevin (ILL) in Grenoble, France.

2. Rheo-SANS measurements in the 1-3 (flow-vorticity) plane

Rheo-SANS experiments in the 1-3 (flow-vorticity) plane were conducted at the NIST Center for Neutron Research on the NGB 10m SANS instrument [55] in the rheometrical geometry described above and previously described [6]. The neutron wavelength, λ, was 5 Å with a wavelength spread $\Delta\lambda/\lambda$ = 12.0%. A detector distance of 5.2 m was used to cover a q-vector ranging from 0.008 Å^{-1} to 0.10 Å^{-1}. Results were corroborated with select rheo-SANS experiments using a Couette geometry with a 1.0 mm gap (R_1= 14.0 mm; R_2 = 15.0 mm; Γ = 36; ε = 0.071). The detector distance of 4.3 m and the neutron wavelength, λ, of 5 Å ($\Delta\lambda/\lambda$ = 12.0%) covered a q-vector ranging from 0.01 Å^{-1} to 0.12 Å^{-1}.

3. Flow-SANS measurements in the 1-2 (flow-gradient) plane

Flow-SANS experiments in the 1-2 (flow-gradient) plane of shear were conducted at the Institut Laue-Langevin over a range of shear rates to cover the shear banding regime and region III. LAOS experiments were performed at a combination of Deborah and Weissenberg numbers such that the shear rate amplitude remained near the transition from region II to region III. All experiments were performed in a short gap Couette cell (5mm path length) with moving inner cylinder R_1 = 25.5 mm and stationary outer stationary R_2 = 26.5 mm (Γ = 5, ε = 0.039) as previously described [6,43,56]. The temperature was held at 35 °C for all experiments. Supplementary steady shear experiments at 33.5 °C showed that temperature did not significantly affect micellar alignment within this range.

The flow-SANS experiments were performed on the D-22 SANS instrument at a detector distance of 11.0 m with an 8.0 m rectangular collimation (40 x 55 mm), 6 Å neutrons, and a wavelength spread of $\Delta\lambda/\lambda = 10\%$. To gain spatial resolution, a stepper motor is used to translate a slit of a desired width across the 1.0 mm gap. LAOS experiments were performed at two gap positions (r/H = 0.25 and 0.75) with a 0.3 mm wide curved slit, and five gap positions (r/H = 0.15, 0.35, 0.5, 0.65, 0.85) with a 0.1 mm wide curved slit. Steady shear experiments were conducted using the 0.1 mm curved slit for a minimum of 10 minutes. All experiments covered a q-range of 0.0048 Å^{-1} to 0.068 Å^{-1}, consistent with previous work on these solutions [6]. Sample transmission measurements were taken at each gap position; gap position did not significantly affect sample transmission. The sample was allowed to equilibrate after loading, and several static measurements were repeated throughout the course of the experiment to ensure that no permanent changes to the sample resulted from shear. LAOS experiments were repeated at each gap position to ensure that the steady alternance structure was measured, and to ensure that the sample had not been subjected to bubbling, evaporation, or irreversible changes from shear. Data was analyzed and reduced using LAMP and the ILL Grasp software. Additional information about the time-resolved measurements can be found in the Supporting Information.

IV. RESULTS

A. Rheology

1. Linear viscoelastic (LVE) regime rheology

Linear viscoelastic (LVE) regime rheology was performed to determine the relaxation and breakage times, τ_{break}, in addition to other properties. As seen in Figure 1, τ_R is determined by the inverse of the crossover frequency between G' and G'', and τ_{break} is estimated by the inverse of the high frequency minimum in G'' [45]. The LVE data was fit with the Oldroyd-B model, where G'' is augmented with a high rate viscosity to account for Rouse modes at higher frequencies. As seen in Figure 1, the results compare favorably with the model, indicating that possible branching does not significantly affect the LVE behavior.

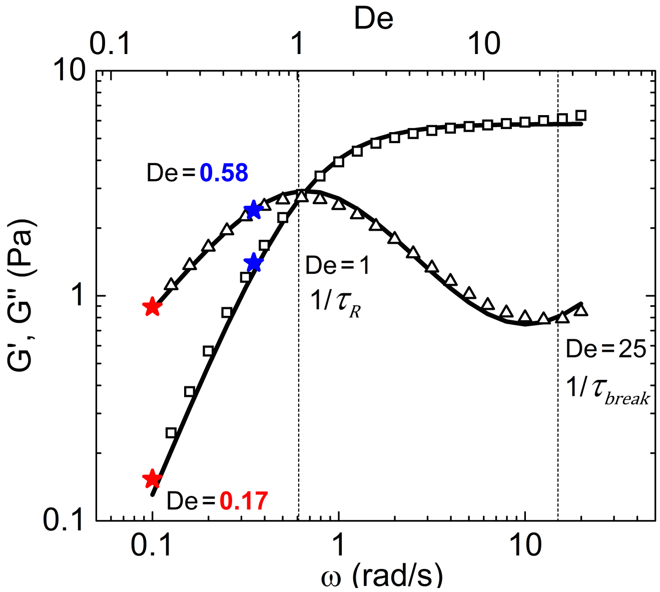

FIG. 1. Dynamic moduli G' (□) and G'' (△) of the 0.05% wt NaTos WLM solution. The Oldroyd-B model fit is shown by solid line. The two Deborah numbers that will be examined by LAOS section are highlighted in red (De = 0.17, ω = 0.1 rad · s^{-1}) and blue (De = 0.58, ω = 0.35 rad · s^{-1}).

The largest deviations are seen in at high frequencies: a true plateau modulus, G_N^0, is not achieved as G' displays a mild slope, and the location of G''_{min} is incorrectly predicted. Deviations at low frequency are also

TABLE I. Average characteristic properties of the 0.05% wt NaTos WLM solution

Property	**Notation**	**Method**	**Value**
Relaxation time	τ_R (s)	LVE rheology	1.7 ± 0.1
Zero-shear viscosity	η_0 (Pa·s)	Cross model	9.5 ± 1.0
High shear viscosity	η_∞ (Pa·s)	Oldroyd-B model	0.04 ± 0.01
High shear viscosity	η_∞ (Pa·s)	Cross model	0.03 ± 0.01
Power law index	N	Steady shear rheology	0.07 ± 0.01
Critical shear rates	Wi_1, Wi_2	Startup rheology, model fits	2.6 ± 0.6, 100 ± 10
Plateau modulus	G_{N}^0 (Pa)	LVE rheology	6.4 ± 0.4
Minimum loss modulus	G''_{min} (Pa)	LVE rheology	0.76 ± 0.07
Breakage time	τ_{break} (s)	LVE rheology/model fits	0.07 ± 0.01
Reptation time	τ_{rep} (s)	LVE rheology/model fits	40 ± 5
Mesh size	ξ_M (Å)	model fits	870 ± 20
Entanglement length	l_e (Å)	model fits	890 ± 40
Contour length	L_c (Å)	model fits	7500 ± 500
Cross-sectional radius	r_{cs} (Å)	SANS flexible cylinder model	20.8 ± 0.4
Persistence length	l_p (Å)	Schubert *et al.* [4] (in H_2O)	850 ± 10

seen in G'. As LAOS shear banding has been previously studied in entangled polymers at $De > 1$, we focus on $De < 1$. The frequencies De = 0.17 and De = 0.58 are highlighted, where the primary LAOS experiments were performed. Using the LVE data, the crossover frequency, ω_c = 0.6 rad·s^{-1}, resulting in τ_R = 1.7 s. Table I provides an estimate of the average length and time scales of the solution and uncertainties for multiple sample preparations, determined from rheology, SANS, and model fits [4, 45, 57–60]. The value of the persistence length, l_p, was determined by Schubert *et al.* [4] via flow-birefringence measurements for the sample prepared in water, which should be comparable to that of the current system prepared in D_2O [61].

2. Steady shear flow curve and startup measurements

The steady shear flow curve is shown in Figure 2, where the shear rate of the primary LAOS measurements, Wi = 75, is highlighted for reference. As seen by the log-log slope of the viscosity of -0.93, the resulting power law index is N = 0.07. While this non-zero power law index indicates an increasing, monotonic constitutive equation, shear banding is both possible [14,35] and predicted for banding in a cylindrical Couette device [62]. Additionally, the time for the stress response to reach steady state after startup is several minutes, and is longer near the beginning of region II, consistent with the trends seen in other shear banding WLMs [23, 29, 30, 34]. The three regions of the flow curve in Figure 2 are estimated by the dotted vertical lines. The breakage and recombination model of Cates and Candau [45] (Equation 1) yields a critical stress, σ_1 = 2/3G_{N}^0, of 4.03 Pa, which corresponds to a measured critical shear rate of Wi = 1.1. From Equation 1, the theoretical critical shear rate is Wi = 2.6. This discrepancy between the measured and theoretical critical shear rate may be explained by possible branching in the system, as it has been shown previously that the scaling of G_{N}^0 is stronger when branching is not present [47]. Further, the ionic nature of the system, and solution temperature and composition, may play a role [33]. The data past the shear banding regime were fit to the Bingham fluid model, as performed by Salmon *et al.* [49], yielding σ = 4.1 + 0.04Wi. Using this model, we estimate that Wi_2 = 100. The flow curve in Figure 2 is similar to that used in the VCM model predictions [35], providing a quantitative comparison for our experimental results. While differences exist, especially at low Wi, this is likely an effect of the larger gap-to-radius ratio used in their work, such that we expect better agreement at equal ratios [63].

The shear startup measurements used to corroborate the flow curve reveal rich transients as the stress evolves toward steady state shear banding. Hu *et al.* [20] analyzed the transient velocity profiles of shear banding wormlike micelles using PTV, and related the behavior back to the features observed in the startup rheology. The PTV confirmed steady state shear banding for conditions when shoulders and other non-linear features were observed in the time-dependent startup stress response, similar to the features originally documented by Grand *et al.* [29]. When we examine the stress responses of our solution upon startup at shear rates in the shear banding regime, we observe these same features indicative of steady state shear banding: large stress overshoots, shoulders, undershoots and secondary overshoots before the stress reaches its steady state value. The stress transients also persist for hundreds of relaxation times at shear rates within the shear banding regime, again in agreement with experimental signatures of shear banding [23, 29, 30] and modeling predictions [63]. A more detailed study of this startup behavior will be presented in a following manuscript. While we have previously shown that high levels of branching ($C_s \geq 0.10\%$ wt NaTos) inhibit shear band formation [6], any branching in this solution does not suppress shear banding.

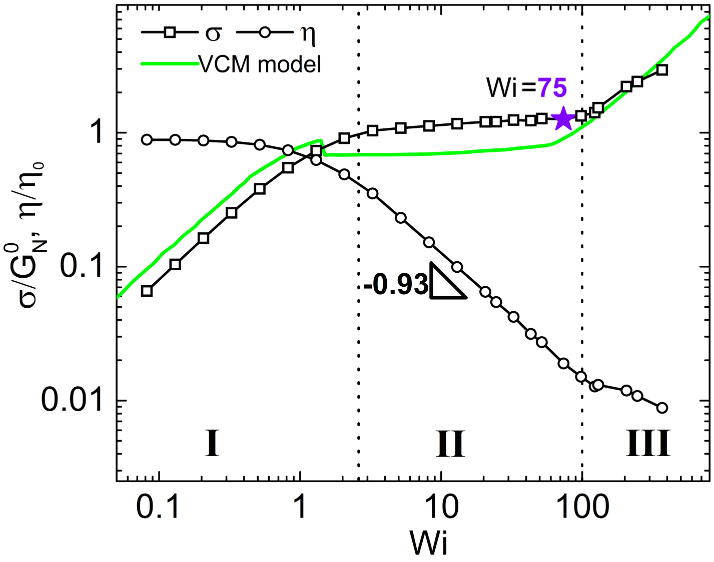

FIG. 2. Steady shear flow curve for the 0.05% wt NaTos solution. Regions I, II and III are estimated using Equation 1 and the Bingham model past region II. The $\star$ indicates the maximum Wi for the majority of the LAOS measurements. Similar features are observed between the experimental data and the VCM model flow curve (digitized from Zhou *et al.* [35]).

3. Large amplitude oscillatory shear (LAOS)

LAOS measurements were performed at many Deborah and Weissenberg number combinations; select results are shown in the Pipkin diagram of the elastic Lissajous-Bowditch curves (σ vs. γ) in Figure 3 (top) and viscous Lissajous-Bowditch curves (σ vs. $\dot{\gamma}$) in Figure 3 (bottom). We focus on $0.17 \leq De \leq 0.75$ and $64 \leq Wi \leq 113$, where the shapes of the elastic and viscous Lissajous-Bowditch projections are fairly similar. The stress responses share many of the same features, including stress overshoots that lead to secondary loops in the viscous Lissajous-Bowditch projections, followed by local stress undershoots and secondary overshoots. While it is difficult to tell from the Pipkin diagrams, many of the LAOS stress overshoots and undershoots are similar to those observed in the stress response to shear startup [20, 23]. The elastic Pipkin diagram shows that with increasing De at constant Wi, the stress overshoot gradually disappears. This overshoot is an indication of micellar breakage, which often leads to shear banding [64]. We postulate that at sufficiently high frequencies, shear banding will cease or a non-breakage shear banding mechanism will occur, in agreement with the predictions of Zhou *et al.* [35]. However, as the stress responses within our range share qualitatively similar features, the possibility of shear banding during LAOS is difficult to determine from the shear stress alone. See the Supporting Information for a direct comparison of LAOS conditions, reproducibility studies, and the uncertainty associated with the features.

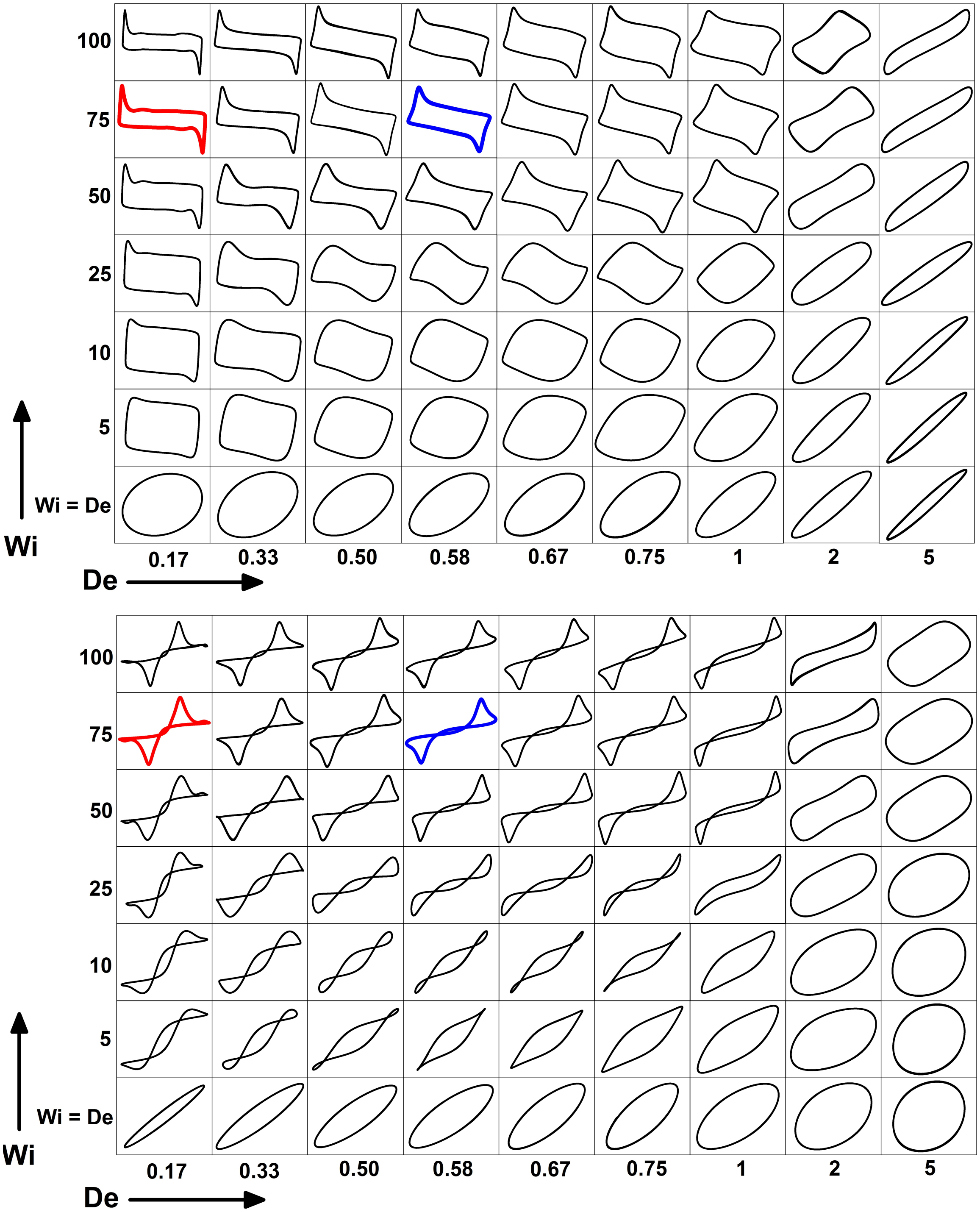

FIG. 3. Pipkin diagrams of the Lissajous-Bowditch projections: (top) Elastic ($\sigma(t)$ vs $\gamma(t)$) and (bottom) viscous ($\sigma(t)$ vs $\dot{\gamma}(t)$). The bolded red and blue spectra correspond to the conditions explored using flow-SANS.

The primary SANS experiments are highlighted in Figure 3 (De = 0.17, Wi = 75; De = 0.58, Wi = 75), where a large stress overshoot is observed in both cases. The overshoot appears more pronounced when De = 0.17; however, the magnitude of the stress overshoot (maximum stress during the cycle) is smaller at this condition (23.2 ± 0.2 vs. 28.6 ± 0.2 Pa). The other major difference between the curves is accentuated in the elastic Pipkin diagram. At De = 0.17, the stress response after the overshoot appears relatively constant and is nearly flat with decreasing strain, whereas at De = 0.58, the stress is continuously evolving. Finally, the stress response at De = 0.17, Wi = 75 is nearly in phase with the applied shear rate, indicating that the response is primarily shear rate-dependent. At De = 0.58, Wi = 75, the stress response is also primarily shear rate-dependent but shows a slight phase shift. This phase shift indicates that the stress response is more elastically-dominated than in the first condition, leading to a larger stress overshoot. These features are not surprising, as the frequency is three-fold that of the first condition, and the LVE elastic modulus at this frequency is an order of magnitude larger than that of the first condition. The dominant stress overshoot at both conditions gives credence to the 'sequence of physical processes' approach of Rogers and co-workers for analyzing LAOS, as the cycle is dominated by fluid-like behavior in both conditions when $De < 1$, but also contains elastic contributions [65–67]. The presence of stress overshoots may lead to transient and steady state shear banding in polymers and WLMs due to breakage [64]; thus we anticipate that the more prominent overshoot, and thereby higher degree of breakage, when De = 0.58 should lead to more pronounced shear banding.

B. Static SANS

Static small angle neutron scattering was performed in all configurations (static quartz cells, two rheometer configurations, and 1-2 shear cell) to determine the equilibrium microstructures and micellar length scales, and to verify that the structure is independent of sample geometry. The 1-D azimuthally-averaged SANS data and a sample 2-D static scattering pattern are shown in Figure 4, in the full q-range from 0.003 Å^{-1} to 0.5 Å^{-1} (real space dimensions ≈ 10 Å to 6000 Å). At rest, the 2-D pattern is isotropic with regard to angle, indicating no net micellar orientation. A mild interaction peak occurs at q ≈ 0.02 Å^{-1} from the partial screening of electrostatic interactions with NaTos addition, indicative of a preferred separation distance between micelles. The peak, which remains at the same q-value, is more pronounced at lower salt concentrations and disappears with higher salt concentrations due to further screening of the electrostatic interactions [6]. SANS results were used to calculate the micellar length scales seen in Table I at q-values greater than the interaction peak, which favorably compared to previous cryo-TEM estimates and SANS fits [6] and the length scales determined by Schubert *et al.* [4]. The cross-sectional radius, r_{cs}, was 20.8 Å using the flexible cylinder model, which lies between the calculated radii in solutions with less salt (21.3 Å) and more salt (20.4 Å) [6]. The slight decrease in cross-sectional radius with added salt is expected, as screening around the surfactant headgroups leads to a smaller effective headgroup size.

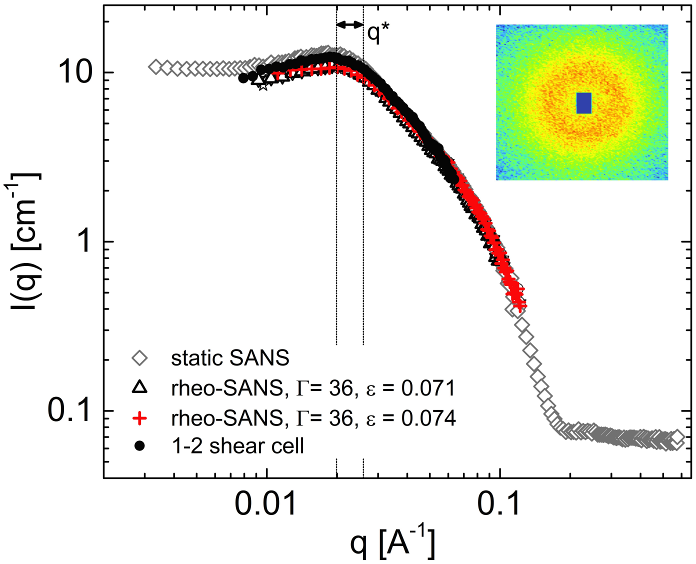

FIG. 4. Static SANS measurements of the 0.05% wt NaTos solution in all configurations. Excellent agreement is seen between the static quartz cells, rheometer configurations, and 1-2 shear cell despite differences in geometry, detector distance, path length and wavelength. The static 2-D pattern from the 1-2 shear cell is shown, where the faint ring leads to the mild interaction peak in the 1-D scattering.

C. Steady shear SANS

As the rheological results were indicative of shear banding, SANS measurements were performed to determine the projections of the shear-induced microstructures in two planes, and to compare them to the measured rheology. WLM segments flow-align under shear [44], and we quantify these microstructural rearrangements by a scalar alignment factor [68] and angle of alignment calculated from the 2-D SANS patterns. Note that in the case of 1-3 plane rheo-SANS, $\phi_0 = 0$ due to the symmetry imposed by the method. For all SANS experiments, the resulting microstructural rearrangements are quantified by the anisotropy in the scattered intensity, in the q^{-1} (rod-like segment) scattering regime, denoted by q^* (Figure 4):

$$A_f(q^*) = \frac{\int_0^{2\pi} I(q^*,\phi)\cos(2(\phi-\phi_0))\,\mathrm{d}\phi}{\int_0^{2\pi} I(q^*,\phi)\,\mathrm{d}\phi} \tag{3}$$

where $I(q^*, \phi)$ is the azimuthal intensity over q^*, and ϕ is the azimuthal angle and ϕ_0 is the angle of maximum intensity. See Supporting Information for a plot of the anisotropic intensity distribution, q-range determination, and uncertainty associated with the A_f calculations.

1. 1-2 plane flow-SANS

Spatially-resolved, 1-2 plane flow-SANS measurements were performed at applied shear rates in regions II and III: Wi = 14, 25, 44, 63 and 75 (region II), 97 (border of region II and III), 130 and 247 (region III). Figure 5 shows the 2-D scattering patterns and 1-2 plane alignment factor, referred to as 1-2 A_f in all figures, as a function of gap position, r/H, and shear rate. Scattering patterns are shown for three shear rates: Wi = 25 (region II), Wi = 75 (end of region II), and Wi = 247 (region III). As the alignment factor is a function of local shear rate [6], lines between points are for visual aid only, because the shear rate may change across the band and is not always a linear function of gap position. One trend is immediately apparent in the spatially-dependent alignment factor for the shear rates within region II. While the inner wall alignment factor, $A_f(r/H = 0.15)$, steadily increases with increasing applied shear rate, the outer wall alignment factor, $A_f(r/H = 0.85)$, remains fairly constant and near zero. Visually, this results in nearly isotropic scattering patterns at r/H = 0.85 when Wi = 25 and 75 (Figure 5). The large drop in A_f with increasing r/H, which is clearly seen in the 2-D patterns, indicates a discontinuous alignment profile. This trend in alignment is expected, as the shear rate profile is discontinuous across the gap [20] and is similar to the alignment trends seen in other shear banding WLM solutions [27]. Conversely, for shear thinning (region III), the material structure is similar across the gap, as evidenced by the 2-D scattering patterns when Wi = 247. In region II, the slope of the alignment factor between $r/H = 0.15$ and $r/H = 0.5$ is roughly equal despite the increasing applied shear rate. This indicates a similar shear rate profile in the high shear band with increasing applied shear rate, which is expected based on Equation 2. The critical alignment factor at the shear band interface, A_f^*, determined by Helgeson *et al.* [25] is A_f^* = 0.18, which indicates that the alignment in the high and low shear bands should be above and below A_f^*, respectively, which is in good agreement with our region II results.

As expected from the rheology, Wi = 75 is still well within the banding regime. The outer wall alignment is similar to that of the other shear rates within the banding regime and is less than A_f^*. At Wi = 97, the outer wall alignment is noticeably higher than that of the lower shear rates but still below A_f^*, and the alignment factor profile is nearly linear. In previous work by Helgeson *et al.* [26] and Gurnon *et al.* [27], the alignment factor (and velocity profile) became increasingly linear as region III was approached, indicating that Wi = 97 is near the onset of region III. When Wi = 130, the alignment at the outer wall (A_f = 0.2) is significantly higher than in the region II shear rates, and is above A_f^*. Further, the alignment factor across the gap appears to have a convex shape, similar to alignment trends at the onset of region III observed by Helgeson *et al.* [26] and Gurnon *et al.* [27]. Lastly, at Wi = 247, $A_f \geq$ 0.40 at all gap positions. The outer wall alignment is 70% of the inner wall alignment, suggesting that a highly ordered material has filled the gap, and that the material is near its maximally aligned state. These trends in the alignment confirm that the onset of region III is between Wi = 97

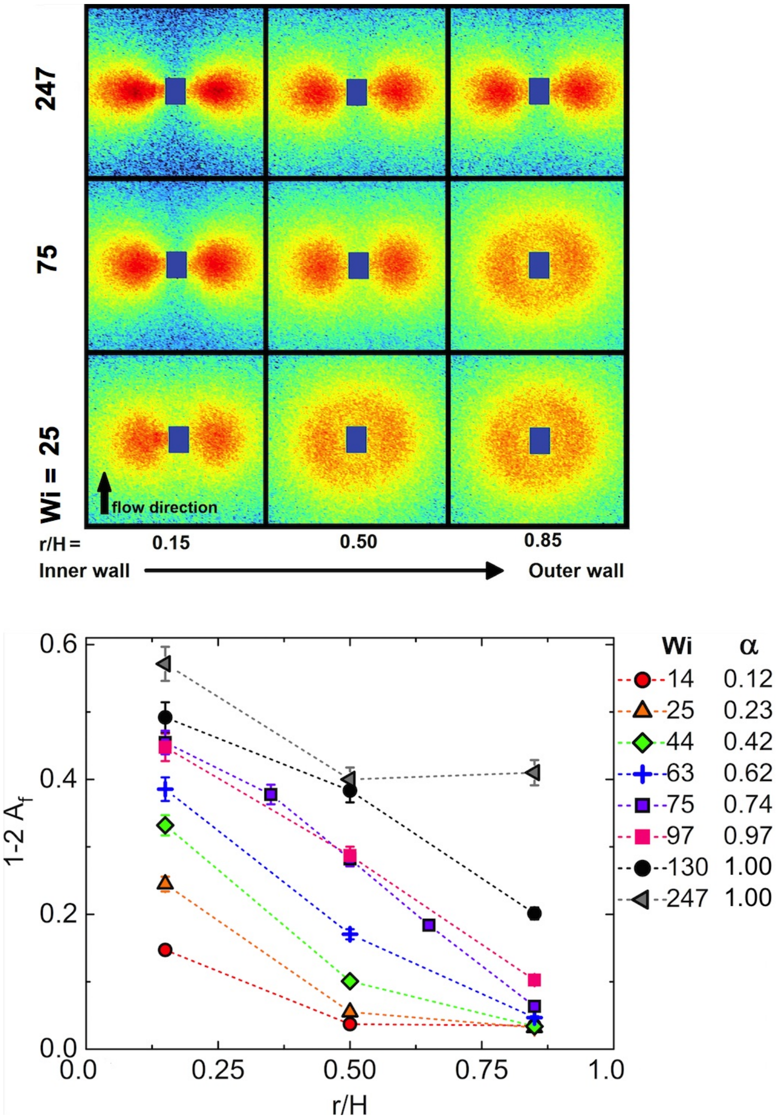

FIG. 5. Steady shear results: 1-2 plane alignment factor and scattering patterns as a function of gap position, r/H, and applied shear rate, Wi. 2-D patterns are shown for Wi = 25 (region II), Wi = 75 (end of region II) and Wi = 247 (region III). Significant decreases in A_f from the inner to outer wall are most prevalent for Wi well within region II. In and near region III, the alignment factor decreases more linearly with gap position. The estimated width of the high shear band, α, is shown in the legend. Dotted lines are for visual aid only.

and Wi = 130, and are in good agreement with the critical shear rate estimates of Wi_1 = 2.6 and Wi_2 = 100.

Using the critical shear rates and Equation 2, the proportion of material within the high shear band, α, was estimated (legend of Figure 5). Note that α was not significantly impacted by choice of Wi_1 = 2.6 versus Wi_1 = 1.1. At Wi = 75, the proportion of material within the high shear band was estimated to be 75%, whereas at Wi = 97, 97% of the material was in the high shear band. These α values agree well when the alignment factor near the calculated band interface is compared to A_f^*. When $Wi \leq 75$, the outer wall alignment factor (r/H = 0.85) is fairly independent of the applied shear rate, suggesting that the shear rate within the low shear band is roughly equivalent at these applied shear rates. Conversely, the higher outer wall alignment at Wi = 97 at may indicate an increase in the average shear rate in the band [26, 27]. The calculated band width of 75% at Wi = 75 also agrees well with time-resolved 1-2 plane SANS data at Wi = 75. These measurements, performed at steady state, are able to detect the presence or absence of fluctuations in the material response, as measured by the alignment factor (see Supporting Information). The alignment factor at r/H = 0.15, 0.35 and 0.50 is nearly constant in time and does not exhibit fluctuations. The alignment at r/H = 0.65 and 0.85, however, exhibits fluctuations. These fluctuations are likely the result of the proximity of the measurement to the shear band interface, and fluctuations of the shear band interface and oscillating rheological responses that can result in shear banding fluids [31–34]. As both positions exhibit alignment fluctuations, the shear band interface is inferred to be between r/H = 0.65 and 0.85, in good agreement with the calculated α = 0.75. While we are below the critical Taylor number for elastic turbulence ($Ta_c \approx 22$) in the shear banding regime [69,70], interface fluctuations are to be expected in shear banding WLMs and vortices in the vorticity direction are also possible [31, 32]. However, due to the low concentration, small gap-to-radius ratio of the shear cell, high temperature, and small amplitude of the alignment factor oscillations, it is likely that the deformations and undulations of the shear band interface are also of small amplitude [33].

2. 1-3 plane rheo-SANS

Rheo-SANS experiments complement the 1-2 plane results, where the 1-3 plane alignment factor versus shear rate is shown in Figure 6 for two rheometer configurations. The 1-3 plane alignment increases steadily with shear rate until Wi = 250, at which point the measured alignment becomes independent of applied shear rate. As Wi = 250 is well within region III, the constant alignment with increasing shear rate in this region indicates that the material across the gap is nearly uniform. This result agrees well with the 1-2 plane results at Wi = 247, where the outer wall alignment is 70% of the inner wall alignment, and A_f at all gap positions is larger than 0.40. When the material achieves its maximally aligned state in the 1-2 plane, we expect the alignment factor to be nearly constant across the gap [27]. In Figure 6, the 2-D scattering patterns are shown for the same shear rates as in Figure 5. Note that the flow direction is in the horizontal direction with respect to the scattering patterns, as opposed to in the vertical direction as seen in the 1-2 plane patterns.

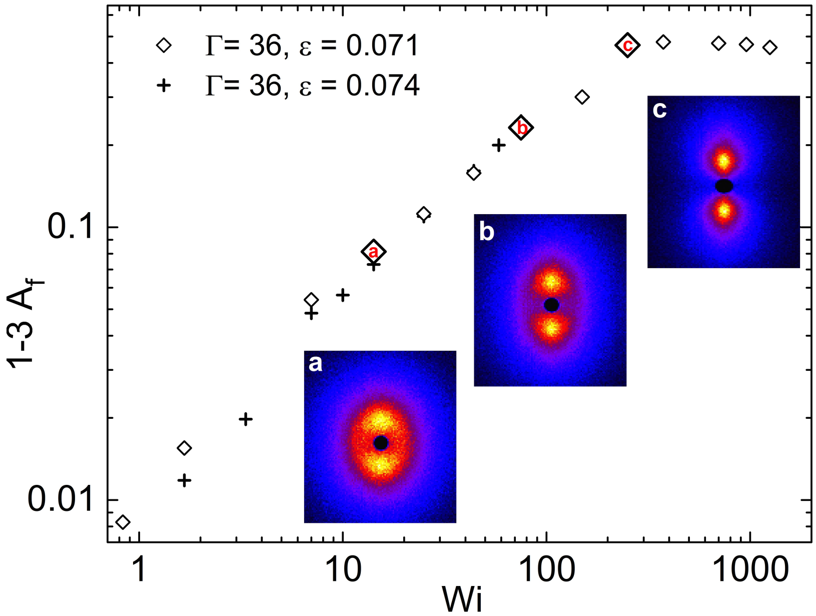

FIG. 6. 1-3 plane A_f as a function of applied Wi. Excellent agreement is obtained between two rheometer configurations and sample preparations. A_f increases with Wi until Wi = 250, at which A_f becomes shear rate independent. Scattering patterns are shown for Wi = 25 (region II, a), Wi = 75 (end of region II, b) and Wi = 250 (region III, c). Evidence of shear banding is seen in (a) and (b), as the anisotropy is superimposed with an isotropic ring in the flow direction; however this ring disappears at Wi = 250.

While the results reported in Figure 6 are the steady state values, the measurements were performed with temporal resolution to capture the startup behavior. In all experiments, at least $200\tau_R$ was required for the alignment factor to reach steady state, consistent with expectations for a shear banding sample [23]. Clear alignment is observed when Wi = 25 (a), as evidenced by the increased intensity in the vorticity direction (z-direction). However, in addition to this alignment, an isotropic background ring is observed at $q \approx 0.02$ Å^{-1}, where the interaction peak is located (red/purple). The pronounced lobes (yellow) superimposed with this isotropic ring have been interpreted as a signature of shear banding by Berret *et al.* [21], as the 1-3 plane scattering is a convolution of the spatially-dependent scattering across the gap. When compared with our 1-2 plane scattering patterns at $Wi = 25$, the lobes in the 1-3 plane pattern clearly result from the pronounced lobes when $r/H = 0.15$ (Figure 5). The nearly isotropic 1-2 plane scattering from the material in the low shear band ($r/H = 0.5, 0.85$) in Figure 5 results in the isotropic portion of the 1-3 plane scattering. The nearly isotropic portion of the scattering is also observed at $Wi = 75$, near the end of region II (Figure 6b). The intensity of the isotropic portion (purple) is much lower and the intensity of the lobes (yellow/red) is much higher at this shear rate, indicating a larger proportion of material within the high shear band. This result is expected, as calculations indicate roughly three-fold more material in the high shear band at this rate. The highest shear rate is well within region III ($Wi = 250$, c), where no shear banding is expected. There is no evidence of the isotropic ring in the scattering, where a highly aligned, butterfly-like pattern is observed. The absence of the isotropic ring is verified by the 1-2 plane data, as the material is highly aligned at all gap positions at $Wi = 250$.

D. LAOS 1-2 plane flow-SANS

The primary LAOS conditions, $De = 0.17$, $Wi = 75$ and $De = 0.58$, $Wi = 75$, have the same shear rate amplitude so the impact of frequency on shear banding could be investigated. Supplementary experiments were performed on conditions ranging between $0.17 \leq De \leq 0.75$ and $64 \leq Wi \leq 113$, where the alignment factor was examined as a function of gap position, r/H, and normalized cycle time, t/T. For all conditions, when $t/T = 0$ and 0.5, the applied strain is zero ($\gamma = 0$) and the magnitude of the shear rate, $|\dot{\gamma}|$, is at a maximum. Conversely, when $t/T = 0.25$ and 0.75, $\dot{\gamma} = 0$ and $|\gamma|$ is at a maximum. As the alignment factor measures the degree of micellar alignment, which is independent of shear direction, we compare the alignment with the *magnitude* of the strain or shear rate when analyzing SANS results. Results are also compared with the predicted shear banding regime of Zhou *et al.* [35] using the VCM model. While the specific parameters used in their work differ from our conditions, the flow curves are similar (Figure 2). Our experimental LAOS conditions are compared to the VCM model predictions in Figure 7. Five of the seven conditions are predicted to shear band under LAOS, and six of the seven displayed steady shear banding at equivalent shear rates. Additional details on the reproducibility of these results can be seen in the Supporting Information.

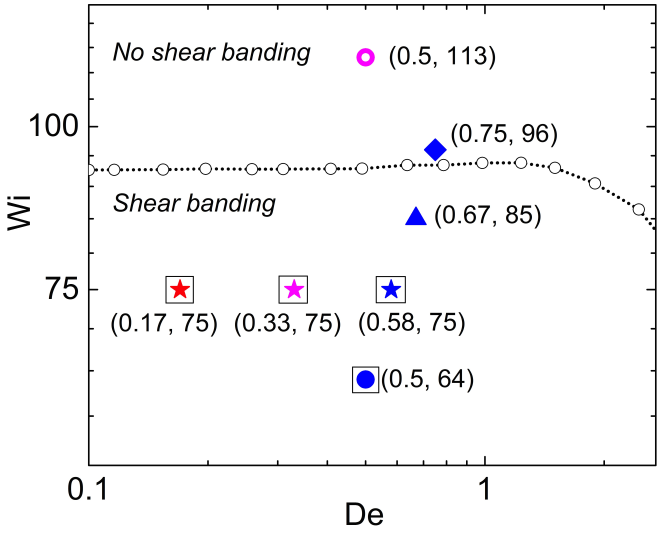

FIG. 7. Comparison of experimental LAOS conditions with VCM model predictions (open circles). Equal strain amplitudes are shown by color, Wi by symbol, and De by open/closed symbols. All but two conditions are predicted to shear band under LAOS. Alignment banding is observed for conditions marked by ☐. VCM predictions are digitized from [35].

1. LAOS Condition 1, De *= 0.17,* Wi *= 75*

In condition one, the sample is expected to exhibit primarily fluid-like behavior throughout the oscillation as $De \ll 1$. Figure 8(a) shows the spatially-dependent alignment factor during the LAOS cycle, where the shape and phase of the response at all gap positions mirrors the magnitude of the applied shear rate. The alignment is at a maximum at the maximum shear rate ($t/T = 0$, 0.5). A comparison of the alignment and the stress response can be seen in Figure 10, where both responses are nearly in phase with the applied shear rate, indicating predominantly viscous behavior through the cycle. Interestingly, the alignment does not appear to be influenced by the applied strain despite the large stress overshoot in the rheology, and shows no response to this stress overshoot (Figure 10). We note that structural changes in the stress overshoot region may occur on larger length scales than accessible by SANS, thus we limit our comparison of the shear-induced structures under LAOS to segmental alignment. Larger-scale structural rearrangements can be detected via rheo-SALS and may result from shear-induced de-mixing [20,27].

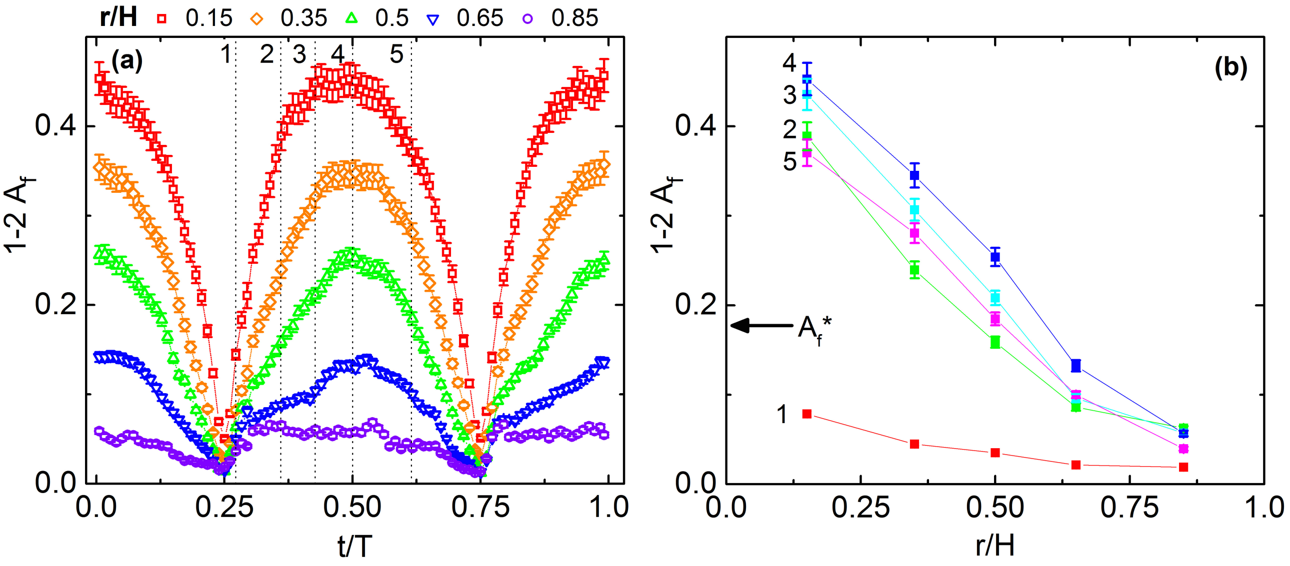

FIG. 8. (a) 1-2 plane A_f as a function of cycle time, t/T, and gap position, r/H, at De = 0.17, Wi = 75. The shape and time-dependence of A_f closely tracks that of $|\dot{\gamma}|$. (b) 1-2 A_f as a function of gap position at select t/T as indicated in (a). The alignment factor as a function of gap position decreases significantly when $A_f > 0$, leading to a similar mechanism of shear banding as is observed under steady shear.

As seen in Figure 8(a), the alignment factor decreases rapidly and monotonically as a function of gap position at all times, which is highlighted during specific portions of the cycle in Figure 8(b). The minimum alignment occurs roughly at times of zero shear rate and maximum strain, which further indicates that the material does not respond to the applied strain on the segment length scale at this condition. The profiles in Figure 8(b) indicate LAOS shear banding, as the outer wall alignment at multiple t/T is significantly lower than the inner wall alignment, and is below the steady shear critical value of A_f^* = 0.18. This trend in the alignment is fairly insensitive to t/T, showing the persistence of the shear banded state through the cycle. The steady decrease in the alignment factor with gap position is similar to the steady shear trends near the end of region II, $Wi \geq 63$. Further into region II ($Wi < 63$), the alignment decreases more significantly and discontinuously near the shear band interface. Thus, shear banding at this LAOS condition is similar to steady shear banding between Wi = 63 and 75 (see Discussion).

2. LAOS Condition 2, De *= 0.58,* Wi *= 75*

As condition two is at a higher frequency than condition one, the sample is expected to show signatures of both viscous and elastic-like behavior during the cycle. The 1-2 plane alignment can be seen in Figure

9(a), where local extrema are observed as a function of time at all gap positions. Similar to condition one, the segmental alignment at all gap positions is in phase with the measured stress response (Figure 10), and is primarily in phase with the applied shear rate. However, in contrast to condition one, at this higher frequency, significant overshoot behavior is evident in the alignment factor after the shearing direction is reversed ($\dot{\gamma} = 0$ at $t/T = 0.25, 0.75$). The local extrema in the alignment factor response are reflective of the local curvature changes in the stress response at this condition (Figure 10). While the stress response exhibits a large stress overshoot and local curvature changes in time that resemble secondary undershoots and overshoots, a true undershoot and secondary overshoot are not observed as seen in condition one (Figure 10).

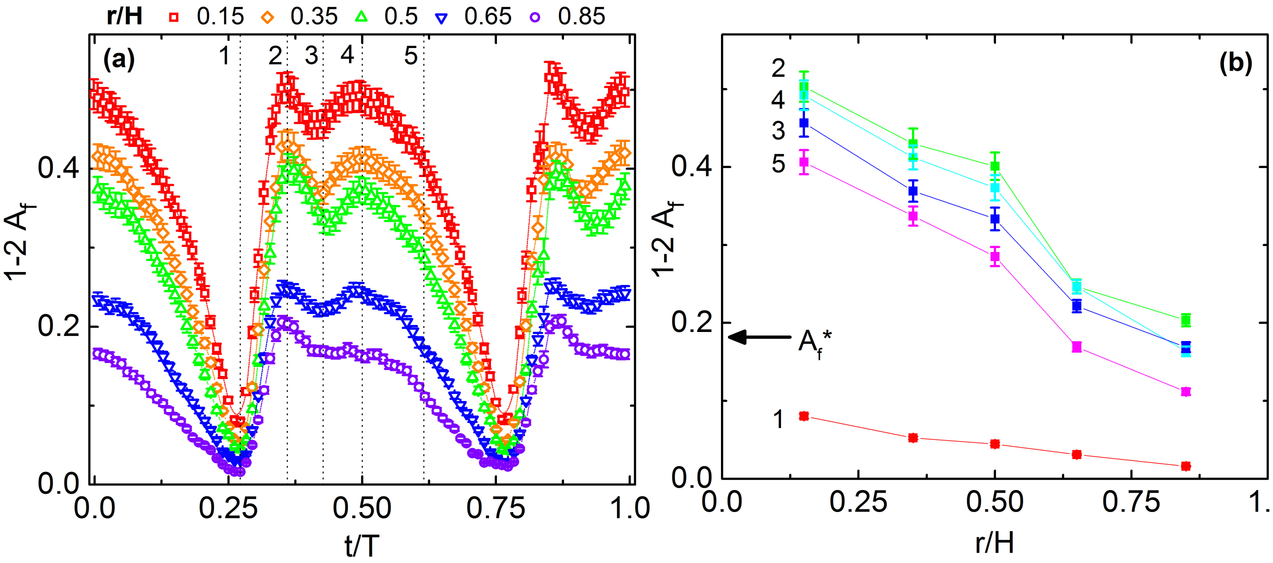

FIG. 9. (a) 1-2 plane A_f at $De = 0.58$, $Wi = 75$. At all r/H, A_f is in phase with the stress response and roughly in phase with $|\dot{\gamma}|$. As the shape of A_f contains local extrema, A_f is a function of both $|\gamma|$ and $|\dot{\gamma}|$. (b) 1-2 plane A_f at select t/T indicated in (a). A_f is more discontinuous across the gap than in condition one, indicating shear banding that is also fairly independent of t/T.

The alignment factor is not at a global maximum when $t/T \approx 0$ and 0.5 in this condition, but is instead at a local maximum. The maximum alignment factor is observed when $t/T \approx 0.36$, the location of the stress overshoot (Figure 10). Even though $De < 1$, this relationship between the structure and the stress overshoot (and thereby the applied strain) shows that during portions of the cycle, the applied strain and the elastic-like properties of the material are predominant contributions to the shear-induced structure. Similar to condition one, the alignment in Figure 9(b) decreases monotonically as a function of gap position; however, when $r/H \leq 0.5$, the material forms a distinct, highly aligned band, and for $r/H > 0.5$, another clear alignment band is discernible (Figure 9(b)). Between $r/H = 0.5$ and 0.65, there is a distinct drop in the magnitude of the alignment between bands, which is similar to the drop in alignment in the steady shear banding regime (region II). This discontinuity indicates the presence of dynamic shear bands and the location of the shear band interface, which will be explored further in the Discussion. These discontinuous alignment trends are fairly independent of t/T, again indicating the persistence of shear banded structure through the cycle.

3. *Comparison of LAOS results*

Both conditions one and two appear to exhibit LAOS shear banding, in line with the VCM model predictions [35]. A comparison of the alignment and shear stress for both conditions can be seen in Figure 10. The condition one maximum alignment is observed at the maximum shear rate ($t/T \approx 0.5$). As $De \ll 1$, this result is not surprising; however, the maximum stress occurs when $t/T = 0.31$. This discrepancy is interesting, as the stress-SANS rule directly relates segmental alignment and angle (1-2 A_f, ϕ_0) and the polymeric stress, $\sigma_{12,p}$ [26]. In this solution, the segments are nearly flow aligned such that the angle of alignment cannot be well-resolved from the 1-2 plane LAOS data. In condition two, the maximum alignment coincides with the maximum stress, suggesting an elastic-like response upon flow reversal during the LAOS cycle. This behavior precedes viscous alignment behavior, where a local alignment maximum is observed at the maximum shear rate, which is similar to that observed at lower frequency in condition one. The local alignment maximum also corresponds with an inflection point in the stress response.

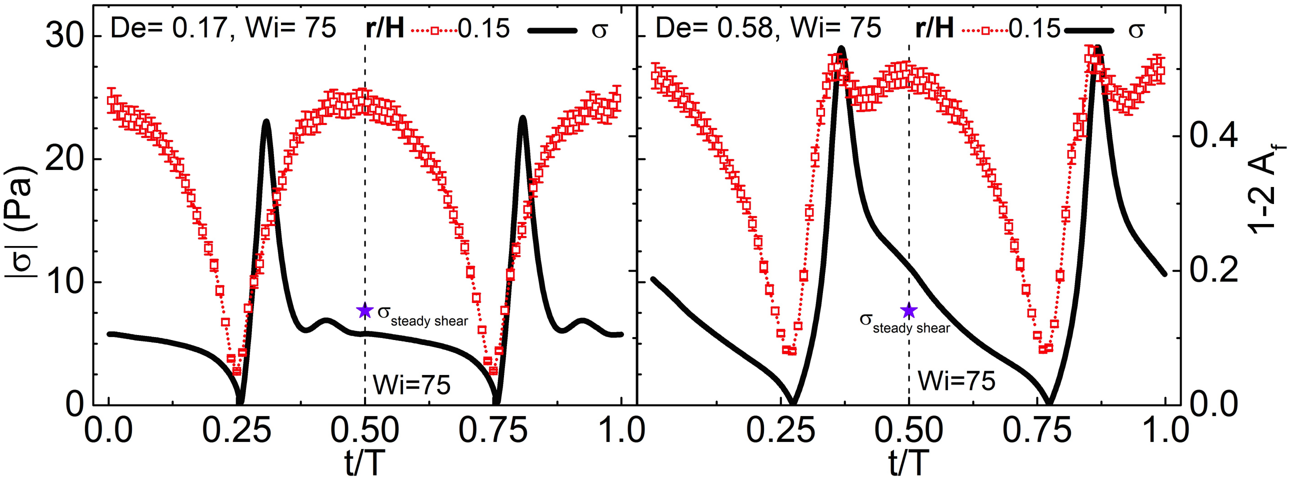

FIG. 10. 1-2 plane $A_f(t/T)$ at r/H = 0.15 and LAOS stress for condition one (L) and two (R); steady shear stress at Wi = 75 given by $\star$. The maximum A_f and stress are greater in condition two. The alignment follows the shape of $|\dot{\gamma}|$ in condition one; whereas the 1-2 A_f in condition two is influenced by the stress response.

In condition two, where the alignment factor shows an undershoot and secondary overshoot, the stress response after the overshoot displays the shoulder-like features described by [20] for shear startup leading to steady state shear banding. The shape of the alignment factor is simple in condition one due to the dominance of fluid-like behavior during the cycle and long cycle time; whereas the shape of the alignment becomes more complicated for condition two, where the frequency is over three times greater, leading to a faster cycle time and a more dominant role of the material elasticity. This is further exemplified when the LAOS stress at Wi = 75 is compared to the steady shear stress in these conditions. In condition one, the LAOS stress is lower than the steady shear stress, as the long period allows the material to relax throughout the cycle. In condition two, the faster cycle time leads to incomplete material relaxation, and thus a higher LAOS stress than steady shear stress at Wi = 75. The higher average stress throughout the cycle in condition two ultimately leads to a higher average 1-2 plane alignment factor during the cycle.

V. DISCUSSION

A. Comparison of LAOS results with steady shear

To further analyze the shear banding under LAOS, the alignment in both conditions was compared to the steady shear alignment. In Figure 11, the 1-2 plane alignment factor is shown for all conditions when Wi = 75 (t/T = 0.5 for LAOS conditions). In condition one (De = 0.17, Wi = 75), the alignment is slightly less than or equal to the steady shear alignment at all gap positions. Conversely, the alignment in condition two is significantly greater than the steady shear alignment, referred to as ‘over-orientation’ as previously termed by Rogers *et al.* [53]. The maximum alignment for condition two (r/H = 0.36) exhibits similar trends in over-orientation, and larger degrees of over-orientation are observed at the outer wall than at the inner wall. In condition one, the similarity of the alignment factor profile with the steady shear profile suggests a similar type of shear banding, where a small portion of the material is in the low shear band. The similar behavior is not surprising when the LAOS stress response is analyzed. Between the point of zero stress ($\sigma(t/T) = 0$) and maximum stress ($\sigma_{max}(t/T)$), the elapsed time is nearly $2\tau_R$ ($\Delta t_1 = 3.20$ s, $\tau_R = 1.67$ s), allowing the material to partially relax during this time. The long cycle time ($T = 62.8$ s) leads to a slow increase in the applied shear rate during the cycle, allowing additional material relaxation. This results in a smaller maximum stress than in condition two (23.2 vs. 28.6 Pa). After the stress overshoot, greater than $7\tau_R$ elapse before the maximum shear rate is reached, giving the material time to relax to a nearly steady state structure. At t/T = 0.5, the shear stress in the LAOS cycle is less than the steady state stress despite Wi = 75 (Figure 10), which leads to the lower LAOS alignment than steady shear alignment observed in Figure 11. The alignment profile in condition one shows a more noticeable discontinuity than the steady shear profile, where the largest difference in alignment occurs at r/H = 0.65. The discontinuous profile resembles those when $Wi < 75$ under steady shear, suggesting that the 'effective' LAOS gap-averaged shear rate at t/T = 0.5 is between $64 < Wi < 75$.

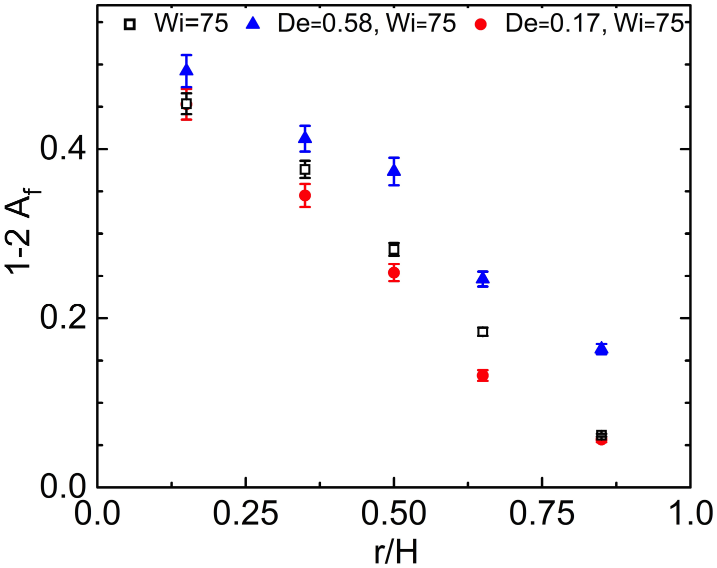

FIG. 11. 1-2 plane A_f at three conditions: Wi = 75 steady shear (□); condition one at Wi = 75 (◯); and condition two at Wi = 75 (△). The condition one alignment is similar, but slightly less than, the steady shear A_f. Condition two exhibits 'over-orientation,' where the 1-2 A_f is always greater than that of steady shear. Over-orientation is more pronounced near the outer wall, in the low shear band.

The significant differences in the alignment factor profile in condition two versus steady shear suggest a different mechanism of LAOS shear banding than seen in condition one. The over-orientation at $t/T = 0.5$ is nearly identical to the over-orientation at $t/T = 0.36$ (global maximum), showing the persistence of the shear banded state throughout the cycle. The large decrease in alignment and clear discontinuity between r/H = 0.5 and r/H = 0.65 indicates that the shear band interface lies between these two gap positions, and that the proportion of material within the high shear band is smaller in this condition ($0.5 < \alpha < 0.65$) than for steady shear ($\alpha \approx 0.75$). However, as the 1-2 alignment factor is a function of shear rate, the effective shear rate within the low shear band must also be higher at this condition. This fits accordingly with the higher stress observed in this condition versus steady shear at $Wi = 75$ (Figure 10). For condition two, the elapsed time between zero stress and the maximum stress is on the order of the relaxation time, $\Delta t_1 = 1.69$ s $\approx \tau_R$ = 1.67 s. Thus, the material has less time to relax than in condition one, resulting in a larger stress overshoot. After the stress overshoot, $Wi = 75$ is reached in $1.4\tau_R$, allowing little additional time for structure relaxation. Shear stresses during the cycle that are higher than the steady shear stress (σ = 7.7 Pa) lead to the observed over-orientation at both t/T = 0.36 (σ = 14 Pa) and t/T = 0.5 (σ = 11 Pa). Condition two therefore leads to a structural metastable shear banded state that is not accessible under steady shear. The chosen Deborah and Weissenberg numbers allow sufficient material relaxation for shear bands to form, but prevent full structure relaxation, resulting in over-orientation. As the over-orientation is more pronounced at the outer wall, the results support the 'disentangle re-entangle' mechanism of shear banding [23], where the material must relax and re-entangle after startup to form the low shear band. With insufficient time for full relaxation and re-entanglement, the low shear band material is trapped in a metastable state of higher alignment.

The differences in the shear banding can be further explained when the alignment between the conditions is compared at all gap positions (see Supporting Information). In regions of increasing shear rate magnitude ($0.25 \leq t/T \leq 0.5$, $0.75 \leq t/T \leq 1$), the alignment significantly differs, which results from the different cycle lengths and amount of material relaxation. In regions of decreasing shear rate magnitude ($0 \leq t/T \leq 0.25$, $0.5 \leq t/T \leq 0.75$), the alignment is nearly identical between the conditions at r/H = 0.15, but deviates with increasing r/H. This suggests that the material at the outer wall must relax much further than at the inner wall during shear banding, again in line with the 'disentangle re-entangle' mechanism of shear banding [23]. The different alignment trends between the conditions enable us to identify different mechanisms of shear banding under LAOS, despite qualitatively similar LAOS stress responses. Condition two exhibits more significant shear banding and a metastable structural state, whereas condition one is able to access stresses below those of the measured steady shear flow curve. These results highlight the importance of using spatially-dependent structure measurements, as shear banding under LAOS could be anticipated from the predictions of Zhou *et al.* [35], but elucidating the mechanism of shear banding requires knowledge of the spatiotemporally varying local microstructure in the bands.

B. Additional LAOS results

Additional flow-SANS experiments under LAOS were performed to determine the effect of frequency and shear rate on LAOS shear banding (Figure 7), and to further validate the VCM model predictions [35]. These experiments were performed using a wider slit (0.3 mm) and were taken at only two gap positions (r/H = 0.25 and 0.75). A comparison of the Lissajous-Bowditch curves for all conditions can be seen in the Supporting Information. Figure 12 shows the shear stress and 1-2 plane alignment factor for De = 0.33, Wi = 75, a frequency between conditions one and two. Not surprisingly, the alignment factor is roughly in phase with the shear rate and follows the phase of the stress response. The maximum alignment occurs when $t/T = 0.5$, similar to condition one; however, evidence of the stress overshoot is observed in the alignment factor, where a local maximum is observed at $t/T \approx 0.34$. For comparison purposes, we interpolate the steady shear alignment factor at r/H = 0.25 and 0.75 at Wi = 75 to be 0.42 and 0.12, respectively. The maximum LAOS alignment is 0.45 and 0.25, respectively. Therefore, over-orientation is minimal at the inner wall, but significant at the outer wall. This result lies between the two initial conditions, and the intermediate deformation frequency gives the material more time to relax during the cycle than in condition two. However, a metastable shear banded state still results because the material cannot relax fully, in line with VCM model predictions (Figure 7).

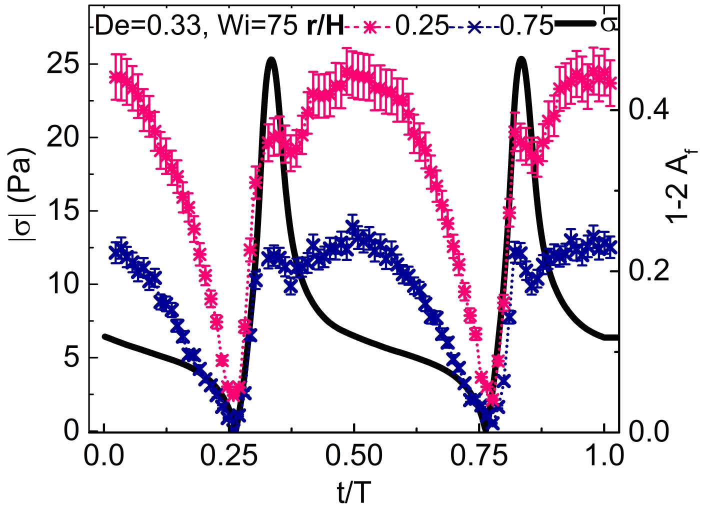

FIG. 12. 1-2 plane A_f and shear stress for De = 0.33, Wi = 75. The alignment during the oscillation contains features of conditions one and two, including an overshoot and maximum alignment when t/T = 0.5.

Next, the strain amplitude from condition two was held constant while the frequency was lowered to obtain a shear rate amplitude well within region II (De = 0.50, Wi = 64). Experiments were also performed at De = 0.50, Wi = 113 to see if shear banding could be induced in region III. The alignment factor and stress for both conditions are shown in Figure 13. The response of the alignment factor is similar between the conditions, and the global maxima in the alignment factor reflect the presence of large stress overshoots in the LAOS stress response. The magnitude of the alignment factor at both gap positions is greater at Wi = 113; however, the stress overshoot has a larger magnitude at Wi = 64. With only two gap positions, it is difficult to precisely determine shear banding; however, shear banding is likely at Wi = 64 due to the similarity in frequency and amplitude to condition two, the shear rate Wi = 64 being well within region II, and the presence of a large stress overshoot. Additionally, a distinct drop in the alignment factor is observed between gap positions, and the alignment at the outer wall ($r/H = 0.75$) is near the critical value of A_f^*. Minimal over-orientation occurs at the inner wall, whereas significant over-orientation occurs at the outer wall. Shear banding is unlikely when Wi = 113. Despite the lower stress overshoot than at $Wi = 64$, the material is highly aligned at both gap positions. The maximum alignment under LAOS at the outer wall is greater than 0.4 and is two-thirds that of the maximum inner wall alignment, suggesting that the shear-induced aligned state has filled the gap. The over-orientation is significant, as the maximum alignment at both gap positions is greater than the steady shear alignment at both Wi = 113 and Wi = 247. The large amplitude and fast cycle time leads to a metastable structural state in region III. The predictions of Zhou *et al.* [35] show De = 0.50, Wi = 64 as shear banding and De = 0.50, Wi = 113 as non-shear banding (Figure 7), in line with our interpretation of the data.

Finally, two conditions were probed where the strain amplitude was held at that of condition two while the frequency was increased, such that De = 0.67, Wi = 84 and De = 0.75, Wi = 95. Both conditions result in shear rate amplitudes that correspond to minimal shear banding under steady shear ($0.03 < \alpha < 0.25$), according to our calculations. The results, shown in Figure 14, are not surprising. A high degree of over-orientation is achieved at both the inner and outer walls for both conditions, indicating that the aligned structure has filled the much of, if not all of, the gap. As the oscillation period is faster than that of condition two and the shear rate is higher in both conditions, the material cannot relax sufficiently during the cycle to form shear bands. As measurements were taken at only two positions, we cannot eliminate the possibility of shear banding but the maximum alignment is so large at the outer wall in both cases that shear banding is highly unlikely. While De = 0.67, Wi = 84 was predicted to shear band by Zhou *et al.* [35], De = 0.75, Wi = 95 was predicted to be outside of the banding regime. As both of these conditions are on the border of the predicted shear banding and non-shear banding regions and the flow curves differ slightly between experiment and prediction (Figure 2), we again obtain good experimental agreement with the VCM model predictions.

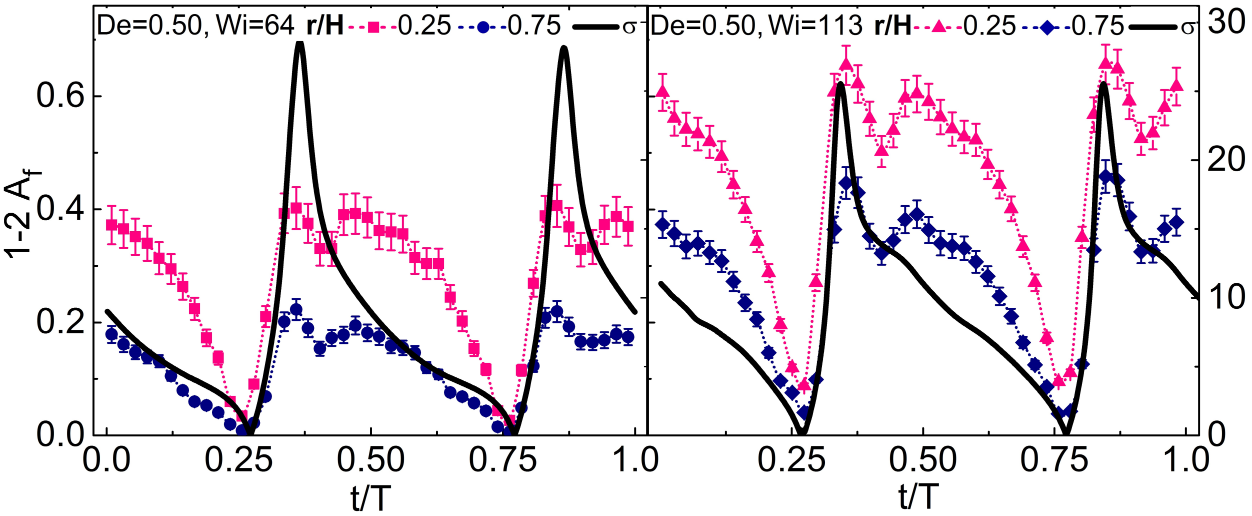

FIG. 13. 1-2 plane A_f and shear stress for De = 0.50, (L) Wi = 64 (region II), and (R) Wi = 113 (region III). (L) The material appears to shear band due to the outer wall over-orientation and large decrease in A_f across the gap. (R) Aligned material has filled the gap, leading to a metastable, non-shear banded state in region III.

Table II gives a comparison of the LAOS conditions, including the maximum stress and corresponding

t/T, the yield strain, the time elapsed from zero stress to the maximum stress (Δt_1), the time elapsed from the stress overshoot to t/T = 0.5 (Δt_2), the maximum over-orientation ratio ($A_{f,\text{max LAOS}}/A_{f,\text{steady shear}}$) at two gap positions, the stress ratio ($|\sigma_{LAOS}|_{avg}/\sigma_{SS}$), and the position t/T of maximum cycle alignment. While showing slight frequency- and amplitude-dependence, the strain acquired between the point of zero shear rate and the stress overshoot is approximately 32 strain units at all conditions, suggesting that this value corresponds to an upper bound on the amount of strain that can be acquired prior to stable flow, such that $\gamma_{yield} = 32.3 \pm 3.1$ [66]. This is typically associated with static yielding, and is referred to here as a yield strain above which flow begins. Using the local modulus analysis approach [65], where the derivative of the shear stress with respect to the strain is calculated as an instantaneous modulus, the value of G' in the stress overshoot region for all conditions was also nearly identical: G'_{local} = 1.2 Pa ± 0.1 Pa. This local elastic modulus corresponds to the elastic modulus obtained in the LVE regime when De = 0.5. Therefore, a rheological analysis alone makes differentiating between LAOS shear banding and shear thinning difficult. In all of the LAOS conditions probed on a basis of Deborah and Weissenberg number, three conditions showed significant over-orientation and are interpreted as non-shear banding: De = 0.5, Wi = 113 (no steady shear banding); De = 0.67, Wi = 85, De = 0.75, Wi = 96. In these conditions, the over-orientation ratio (O-O) at the inner wall was 1.5 or greater, whereas this ratio was 1.3 or less in the shear banding conditions. At the outer wall, the over-orientation ratio was 3.0 or greater, provided that the condition showed steady shear banding. This ratio was 2.9 or less for the LAOS shear banding conditions. These ratios for the degree of over-orientation are similar to those observed in a similar frequency range by Rogers *et al.* [53] in the 1-3 plane (O-O$\approx$1.8); however, LAOS shear banding could not be elucidated from their 1-3 plane measurements. Using the absolute value of the stress during LAOS, a stress ratio was calculated over the steady shear stress, $|\sigma_{LAOS}|_{avg}/\sigma_{SS}$. The ratio was 1.20 or below for LAOS shear banding, and was 1.23 and above for non-shear banding, provided that the condition showed steady state shear banding. These results provide guidelines for LAOS shear banding, assuming steady shear banding as a pre-requisite: O-O(t/T= 0.25) $\leq$ 1.3, O-O(t/T= 0.75) $\leq$ 2.9 and $|\sigma_{LAOS}|_{avg}/\sigma_{SS} \leq$ 1.20. Similarly, for conditions that showed steady shear banding, the cycle times of the stress overshoot and maximum alignment (if not at max Wi) were greater for the conditions that did not shear band.

TABLE II. 0.05% wt NaTos LAOS time scales and properties across conditions. Alignment factors for calculation of the maximum cycle over-orientation (O-O) were interpolated when necessary.

De	**Wi**	Δt_1 **(s)**	Δt_2 **(s)**	σ_{max} **(Pa)**	γ_{yield}	$t/T(\sigma_{max}; A_{f,max})$	O-O$(t/T = 0.25; 0.75)$	$\vert\sigma_{LAOS}\vert_{avg}/\sigma_{SS}$
Shear banding								
0.17	75	3.20	12.06	23.2 ± 0.2	29.1 ± 1.9	0.31 ; 0.50	0.9 ; 0.7	0.87
0.33	75	2.27	4.47	25.3 ± 0.2	30.5 ± 1.4	0.34 ; 0.50	1.1 ; 2.1	1.00
0.5	64	1.96	2.82	28.1 ± 0.5	31.5 ± 1.0	0.38 ; 0.36	1.3 ; 2.9	1.13
0.58	75	1.69	2.36	28.6 ± 0.2	33.3 ± 1.1	0.39 ; 0.36	1.1 ; 2.1	1.20
Non-shear banding								
0.5	113	1.47	3.39	26.7 ± 0.4	32.4 ± 1.4	0.36 ; 0.35	1.6 ; 2.3	1.16
0.67	85	1.52	1.96	27.4 ± 0.3	34.2 ± 1.1	0.40 ; 0.37	1.5 ; 3.0	1.23
0.75	96	1.28	1.85	25.2 ± 0.4	35.4 ± 1.1	0.41 ; 0.39	1.7 ; 3.1	1.25

In non-shear banding conditions, Δt_1 is less than that of the material relaxation time (τ_R = 1.67 s), which explains the high degree of over-orientation. In the latter two conditions, Δt_2 was on the order of the relaxation time, leading to minimal relaxation after the stress overshoot. When the imposed shear conditions correspond to Deborah and Weissenberg numbers of 0.5 and 113, respectively, a pronounced shoulder is reached after the overshoot that leads to the over-orientation in an elapsed time less than that of the relaxation time. As the material does not have time to sufficiently relax throughout the oscillation in all of these conditions, it remains in a highly aligned, metastable state across the gap during LAOS. As Δt_1 and Δt_2 increase, the material has more time to relax through the cycle and the degree of over-orientation decreases. The only condition where over-orientation was not observed was De = 0.17, Wi = 75, where the maximum alignment during LAOS was equal to, or less than, that of the steady state. In most conditions where over-orientation was observed, little over-orientation was seen at the inner wall and significant over-orientation was seen at the outer wall. When Δt_1 is nearly equal to that of the relaxation time and Δt_2 is greater than the relaxation time, over-orientation and shear banding occur simultaneously. A long Δt_1 allows the material to relax partially before the stress overshoot ($De = 0.17, 0.33$), leading to a lower maximum stress. From the results, it is clear that inducing shear banding under LAOS is a delicate balance between the applied Deborah and Weissenberg numbers. If the Deborah number was between 0.17 and 0.58, shear banding was observed under LAOS if the shear rate amplitude was within region II. At higher Deborah numbers in region II and shear rate amplitudes in region III, shear banding was not observed. The interpretation of shear banding and non-shear banding in all of our results agrees well with the predictions of Zhou *et al.* [35] based on Deborah and Weissenberg number. While Adams and Olmsted [14] did not probe conditions where the Deborah number was less than one, these experimental results appear consistent with their predictions based on the Weissenberg number range for shear banding at a Deborah number of one. These results also suggest that any level of branching at this salt concentration does not significantly affect the shear banding behavior.

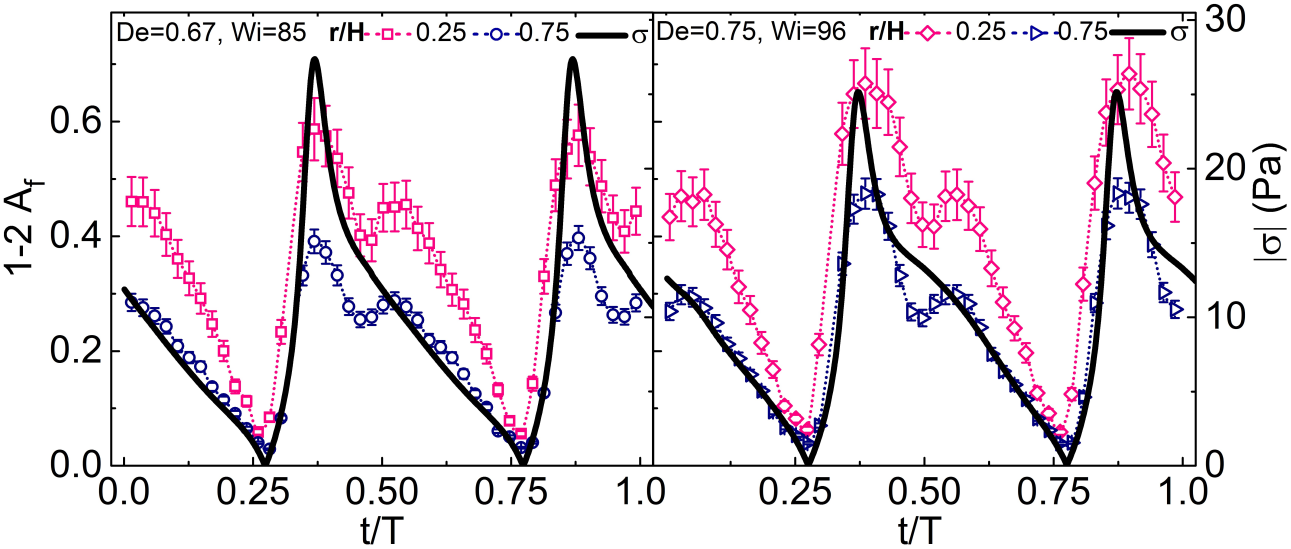

FIG. 14. 1-2 plane A_f and shear stress for conditions where γ_0 = 128.5. (L) De = 0.67, Wi = 84. (R) De = 0.75, Wi = 95. While the magnitude of the alignment differs, the qualitative trends indicate a metastable structural state in region III.

VI. CONCLUSIONS

Shear banding under steady and dynamic deformation was investigated for a model wormlike micelle solution, with steady shear rheology similar to that employed by the VCM model so as to test the predictions of LAOS shear banding. The conditions imposed under LAOS greatly affect the existence and type of shear banding near the onset of region III. We find alignment banding indicative of shear banding for a range of frequencies and amplitudes which are consistent with VCM model predictions. At De = 0.17 and Wi = 75, the maximum alignment as a function of gap position mirrors the steady shear alignment values, indicating a similar shear banding behavior between LAOS and steady shear. At De = 0.58 and Wi = 75, the maximum alignment under LAOS surpasses that of steady shear, termed 'over-orientation.' This over-orientation results from the shorter period of oscillation, which does not give the material sufficient time to relax within the cycle, making the shear banding more pronounced. Further increasing the frequency while keeping the shear rate amplitude constant leads to non-shear banded, metastable structural states in region III. These results have helped experimentally verify predictions of shear banding under LAOS using a mechanistic model that includes shear-induced micellar breakage, and can be used for the improvement of theoretical models.

ACKNOWLEDGMENTS

The authors acknowledge the support of the National Institute of Standards and Technology, U.S. Department of Commerce, and the Institut Laue-Langevin in Grenoble, France in providing the neutron research facilities used in this work. This manuscript was prepared under cooperative agreement 70NANB12H239 from NIST, U.S. Department of Commerce. The statements, findings, conclusions and recommendations are those of the author(s) and do not necessarily reflect the view of NIST or the U.S. Department of Commerce. We thank Miguel Gonzalez (ILL) for designing the time-resolved SANS data processing, and Katie Weigandt (NIST) for help with the rheo-SANS software.

References

[1] Spenley, N. A., M. E. Cates, and T. McLeish, “Nonlinear rheology of wormlike micelles,” Phys. Rev. Lett. **71**, 939–942 (1993).

[2] Berret, J.-F., D. C. Roux, and G. Porte, “Isotropic-to-nematic transition in wormlike micelles under shear,” J. Phys. II **4**, 1261–1279 (1994).

[3] Makhloufi, R., J. Decruppe, A. Ait-Ali, and R. Cressely, “Rheo-optical study of worm-like micelles undergoing a shear banding flow,” Europhys. Lett. **32**, 253–258 (1995).

[4] Schubert, B. A., E. W. Kaler, and N. J. Wagner, “The microstructure and rheology of mixed cationic/anionic wormlike micelles,” Langmuir **19**, 4079–4089 (2003).

[5] Sachsenheimer, D., C. Oelschlaeger, S. Müller, J. Küstner, S. Bindgen, and N. Willenbacher, “Elongational deformation of wormlike micellar solutions,” J. Rheol. **58**, 2017–2042 (2014).

[6] Calabrese, M. A., S. A. Rogers, R. P. Murphy, and N. J. Wagner, “The rheology and microstructure of branched micelles under shear,” J. Rheol. **59**, 1299–1328 (2015).

[7] Candau, S., and R. Oda, “Linear viscoelasticity of salt-free wormlike micellar solutions,” Colloids Surf. A Physicochem. Eng. Asp. **183**, 5–14 (2001).

[8] Oelschlaeger, C., M. Schopferer, F. Scheffold, and N. Willenbacher, “Linear-to-branched micelles transition: a rheometry and diffusing wave spectroscopy (DWS) study,” Langmuir **25**, 716–723 (2008).

[9] Ziserman, L., L. Abezgauz, O. Ramon, S. R. Raghavan, and D. Danino, “Origins of the viscosity peak in wormlike micellar solutions. 1. mixed catanionic surfactants. a cryo-transmission electron microscopy study,” Langmuir **25**, 10483–10489 (2009).

[10] Gaudino, D., R. Pasquino, and N. Grizzuti, “Adding salt to a surfactant solution: Linear rheological response of the resulting morphologies,” J. Rheol. **59**, 1363–1375 (2015).

[11] Rogers, S. A., M. A. Calabrese, and N. J. Wagner, “Rheology of branched wormlike micelles,” Curr. Opin. Colloid Interface Sci. **19**, 530–535 (2014).

[12] Fielding, S. M., “Complex dynamics of shear banded flows,” Soft Matter **3**, 1262–1279 (2007).

[13] Olmsted, P. D., “Perspectives on shear banding in complex fluids,” Rheol. Acta **47**, 283–300 (2008).

[14] Adams, J., and P. D. Olmsted, “Nonmonotonic models are not necessary to obtain shear banding phenomena in entangled polymer solutions,” Phys. Rev. Lett. **102**, 067801 (2009).

[15] Lerouge, S., and J.-F. Berret, “Shear-induced transitions and instabilities in surfactant wormlike micelles,” Polymer Characterization **230**, 1–71 (2010).

[16] Cappelaere, E., J.-F. Berret, J. Decruppe, R. Cressely, and P. Lindner, “Rheology, birefringence, and small-angle neutron scattering in a charged micellar system: Evidence of a shear-induced phase transition,” Phys. Rev. E **56**, 1869–1878 (1997).

[17] Mair, R. W., and P. T. Callaghan, “Observation of shear banding in worm-like micelles by NMR velocity imaging,” Europhys. Lett. **36**, 719–724 (1996).

[18] Britton, M. M., and P. T. Callaghan, “Two-phase shear band structures at uniform stress,” Phys. Rev. Lett. **78**, 4930–4933 (1997).

[19] Hu, Y. T., and A. Lips, “Kinetics and mechanism of shear banding in an entangled micellar solution,” J. Rheol. **49**, 1001–1027 (2005).

[20] Hu, Y. T., C. Palla, and A. Lips, “Comparison between shear banding and shear thinning in entangled micellar solutions,” J. Rheol. **52**, 379–400 (2008).

[21] Berret, J.-F., D. C. Roux, and P. Lindner, “Structure and rheology of concentrated wormlike micelles at the shear-induced isotropic-to-nematic transition,” Eur. Phys. J. B **5**, 67–77 (1998).

[22] Kadoma, I. A., and J. W. van Egmond, “Shear-enhanced orientation and concentration fluctuations in wormlike micelles: Effect of salt,” Langmuir **13**, 4551–4561 (1997).

[23] López-Barrón, C. R., A. K. Gurnon, A. P. R. Eberle, L. Porcar, and N. J. Wagner, “Microstructural evolution of a model, shear-banding micellar solution during shear startup and cessation,” Phys. Rev. E **89**, 042301 (2014).

[24] Becu, L., D. Anache, S. Manneville, and A. Colin, “Evidence for three-dimensional unstable flows in shear-banding wormlike micelles,” Phys. Rev. E **76**, 011503 (2007).

[25] Helgeson, M. E., M. D. Reichert, Y. T. Hu, and N. J. Wagner, “Relating shear banding, structure, and phase behavior in wormlike micellar solutions,” Soft Matter **5**, 3858–3869 (2009).

[26] Helgeson, M. E., P. A. Vasquez, E. W. Kaler, and N. J. Wagner, “Rheology and spatially resolved structure of cetyltrimethylammonium bromide wormlike micelles through the shear banding transition,” J. Rheol. **53**, 727–756 (2009).

[27] Gurnon, A. K., C. R. López-Barrón, A. P. R. Eberle, L. Porcar, and N. J. Wagner, “Spatiotemporal stress and structure evolution in dynamically sheared polymer-like micellar solutions,” Soft Matter **10**, 2889–2898 (2014).

[28] Liberatore, M. W., F. Nettesheim, P. A. Vasquez, M. E. Helgeson, N. J. Wagner, E. W. Kaler, L. P. Cook, L. Porcar, and Y. T. Hu, “Microstructure and shear rheology of entangled wormlike micelles in solution,” J. Rheol. **53**, 441–458 (2009).

[29] Grand, C., J. Arrault, and M. E. Cates, “Slow transients and metastability in wormlike micelle rheology,” J. Phys. II **7**, 1071–1086 (1997).

[30] Berret, J.-F., “Transient rheology of wormlike micelles,” Langmuir **13**, 2227–2234 (1997).

[31] Lerouge, S., M. Argentina, and J. Decruppe, “Interface instability in shear-banding flow,” Phys. Rev. Lett. **96**, 088301 (2006).

[32] Fardin, M.-A., B. Lasne, O. Cardoso, G. Grégoire, M. Argentina, J.-P. Decruppe, and S. Lerouge, “Taylor-like vortices in shear-banding flow of giant micelles,” Phys. Rev. Lett. **103**, 028302 (2009).

[33] Fardin, M.-A., T. J. Ober, V. Grenard, T. Divoux, S. Manneville, G. H. McKinley, and S. Lerouge, “Interplay between elastic instabilities and shear-banding: three categories of Taylor–Couette flows and beyond,” Soft Matter **8**, 10072–10089 (2012).

[34] Manneville, S., “Recent experimental probes of shear banding,” Rheol. Acta **47**, 301–318 (2008).

[35] Zhou, L., L. P. Cook, and G. H. McKinley, “Probing shear-banding transitions of the VCM model for entangled wormlike micellar solutions using large amplitude oscillatory shear (LAOS) deformations,” J. Non-Newtonian Fluid Mech. **165**, 1462–1472 (2010).

[36] Stickel, J. J., J. S. Knutsen, and M. W. Liberatore, “Response of elastoviscoplastic materials to large amplitude oscillatory shear flow in the parallel-plate and cylindrical-Couette geometries,” J. Rheol. **57**, 1569–1596 (2013).

[37] Fardin, M.-A., C. Perge, L. Casanellas, T. Hollis, N. Taberlet, J. Ortín, S. Lerouge, and S. Manneville, “Flow instabilities in large amplitude oscillatory shear: a cautionary tale,” Rheol. Acta **53**, 885–898 (2014).

[38] Tapadia, P., S. Ravindranath, and S.-Q. Wang, “Banding in entangled polymer fluids under oscillatory shearing,” Phys. Rev. Lett. **96**, 196001 (2006).

[39] Ravindranath, S., and S.-Q. Wang, “Large amplitude oscillatory shear behavior of entangled polymer solutions: Particle tracking velocimetric investigation,” J. Rheol. **52**, 341–358 (2008).

[40] Li, X., S.-Q. Wang, and X. Wang, “Nonlinearity in large amplitude oscillatory shear (LAOS) of different viscoelastic materials,” J. Rheol. **53**, 1255–1274 (2009).

[41] Li, Y., M. Hu, G. B. McKenna, C. J. Dimitriou, G. H. McKinley, R. M. Mick, D. C. Venerus, and L. A. Archer, “Flow field visualization of entangled polybutadiene solutions under nonlinear viscoelastic flow conditions,” J. Rheol. **57**, 1411–1428 (2013).

[42] Dimitriou, C. J., L. Casanellas, T. J. Ober, and G. H. McKinley, “Rheo-PIV of a shear-banding wormlike micellar solution under large amplitude oscillatory shear,” Rheol. Acta **51**, 395–411 (2012).

[43] Gurnon, A. K., P. D. Godfrin, N. J. Wagner, A. P. R. Eberle, P. Butler, and L. Porcar, “Measuring material microstructure under flow using 1-2 plane flow-small angle neutron scattering,” J. Vis. Exp. **84**, e51068 (2014).

[44] Eberle, A. P. R., and L. Porcar, “Flow-SANS and rheo-SANS applied to soft matter,” Curr. Opin. Colloid Interface Sci. **17**, 33–43 (2012).

[45] Cates, M. E., and S. J. Candau, “Statics and dynamics of worm-like surfactant micelles,” J. Phys. Cond. Matter **2**, 6869–6892 (1990).

[46] Spenley, N. A., X. F. Yuan, and M. E. Cates, “Nonmonotonic constitutive laws and the formation of shear-banded flows,” J. Phys. II **6**, 551–571 (1996).

[47] Koshy, P., V. K. Aswal, M. Venkatesh, and P. A. Hassan, “Unusual scaling in the rheology of branched wormlike micelles formed by cetyltrimethylammonium bromide and sodium oleate,” J. Phys. Chem. B **115**, 10817–10825 (2011).

[48] Fielding, S. M., and P. D. Olmsted, “Flow phase diagrams for concentration-coupled shear banding,” Eur. Phys. J. E **11**, 65–83 (2003).

[49] Salmon, J.-B., A. Colin, S. Manneville, and F. Molino, “Velocity profiles in shear-banding wormlike micelles,” Phys. Rev. Lett. **90**, 228303 (2003).

[50] Likhtman, A. E., and R. S. Graham, “Simple constitutive equation for linear polymer melts derived from molecular theory: Rolie–poly equation,” J. Non-Newtonian Fluid Mech. **114**, 1–12 (2003).

[51] Vasquez, P. A., G. H. McKinley, and L. P. Cook, “A network scission model for wormlike micellar solutions: I. model formulation and viscometric flow predictions,” J. Non-Newtonian Fluid Mech. **144**, 122–139 (2007).

[52] Zhou, L., P. A. Vasquez, L. P. Cook, and G. H. McKinley, “Modeling the inhomogeneous response and formation of shear bands in steady and transient flows of entangled liquids,” J. Rheol. **52**, 591–623 (2008).

[53] Rogers, S. A., J. Kohlbrecher, and M. P. Lettinga, “The molecular origin of stress generation in worm-like micelles, using a rheo-SANS LAOS approach,” Soft Matter **8**, 7831–7839 (2012).

[54] Kline, S. R., “Reduction and analysis of SANS and USANS data using IGOR Pro,” Journal of Applied Crystallography **39**, 895–900 (2006).

[55] Porcar, L., D. C. Pozzo, G. Langenbucher, J. Moyer, and P. Butler, “Rheo-small-angle neutron scattering at the National Institute of Standards and Technology Center for Neutron Research,” Rev. Sci. Instrum. **82**, 083902 (2011).

[56] Liberatore, M. W., F. Nettesheim, N. J. Wagner, and L. Porcar, “Spatially resolved small-angle neutron scattering in the 1-2 plane: A study of shear-induced phase-separating wormlike micelles,” Phys. Rev. E **73**, 020504 (2006).

[57] Granek, R., and M. E. Cates, “Stress relaxation in living polymers: results from a Poisson renewal model,” J. Chem. Phys. **96**, 4758–4767 (1992).

[58] Granek, R., “Dip in G'' of polymer melts and semidilute solutions,” Langmuir **10**, 1627–1629 (1994).

[59] de Gennes, P. G., Scaling Concepts in Polymer Physics (Cornell University, New York, 1979).

[60] Doi, M., and S. Edwards, The Theory of Polymer Dynamics (Claredon, Oxford, 1986).

[61] López-Barrón, C. R., and N. J. Wagner, “Solvent isotope effect on the microstructure and rheology of cationic worm-like micelles near the isotropic-nematic transition,” Soft Matter **7**, 10856–10863 (2011).

[62] Olmsted, P. D., O. Radulescu, and C. Y. D. Lu, “Johnson–Segalman model with a diffusion term in cylindrical Couette flow,” J. Rheol. **44**, 257–275 (2000).

[63] Zhou, L., G. H. McKinley, and L. P. Cook, “Wormlike micellar solutions: III. VCM model predictions in steady and transient shearing flows,” J. Non-Newtonian Fluid Mech. **211**, 70–83 (2014).

[64] Moorcroft, R. L., and S. M. Fielding, “Shear banding in time-dependent flows of polymers and wormlike micelles,” J. Rheol. **58**, 103–147 (2014).

[65] Rogers, S. A., B. M. Erwin, D. Vlassopoulos, and M. Cloitre, “A sequence of physical processes determined and quantified in LAOS: Application to a yield stress fluid,” J. Rheol. **55**, 435–458 (2011).

[66] Rogers, S. A., and M. P. Lettinga, “A sequence of physical processes determined and quantified in large-amplitude oscillatory shear (LAOS): Application to theoretical nonlinear models,” J. Rheol. **56**, 1–25 (2012).

[67] Rogers, S. A., “A sequence of physical processes determined and quantified in LAOS: An instantaneous local 2D/3D approach,” J. Rheol. **56**, 1129–1151 (2012).

[68] Walker, L. M., and N. J. Wagner, “SANS analysis of the molecular order in poly (γ-benzyl l-glutamate)/deuterated dimethylformamide (PBLG/d-DMF) under shear and during relaxation,” Macromolecules **29**, 2298–2301 (1996).

[69] Perge, C., M.-A. Fardin, and S. Manneville, “Inertio-elastic instability of non shear-banding wormlike micelles,” Soft Matter **10**, 1450–1454 (2014).

[70] Fardin, M.-A., C. Perge, N. Taberlet, and S. Manneville, “Flow-induced structures versus flow instabilities,” Phys. Rev. E **89**, 011001 (2014).